

# Hydrothermal Plume Near-Field Dynamics from LES and Observations

Cyprien Lemaréchal<sup>1</sup>, Guillaume Roulet<sup>1</sup>, Jonathan Gula<sup>1,2</sup>

<sup>1</sup>Univ Brest, CNRS, Ifremer, IRD, Laboratoire d'Océanographie Physique et Spatiale (LOPS), IUEM,  
F29280, Plouzané, France

<sup>2</sup>Institut Universitaire de France (IUF), Paris, France

## Key Points:

- Hydrothermal plumes exhibit strong mixing reflected by significant vertical and temporal variability in entrainment rate in the near-field
- Plume theory cannot be applied directly since forced and lazy plumes are in a transitional state at the scale of hydrothermal edifices
- Short exposure times to high temperatures suggest that biological materials can be transported through the plume without lethal effects

---

Corresponding author: Guillaume Roulet, [roulet@univ-brest.fr](mailto:roulet@univ-brest.fr)

## Abstract

Hydrothermal plumes play a crucial role in vent fields by injecting significant buoyancy flux from centimeter-scale vents and rising hundreds of meters, yet their near-field dynamics remain poorly understood. Using a Large-Eddy Simulation approach with adaptive mesh refinement, we study these plumes at centimeter-scale resolution within a 6 m domain above the vent. We first study a typical black smoker in the forced plume regime to quantify the mean flow and spatial variability, investigating the link between turbulent structures and the entrainment rate  $\alpha$  of surrounding water. Significant vertical and temporal variability in  $\alpha$  is observed, with an overall value of  $\alpha = 0.19$ . The results are compared with in-situ data and plume theory. Next, we investigate the sensitivity of the flow field to source parameters, characterizing the transition between forced or lazy plume regimes and the pure plume regime. In the far-field, plumes achieve self-similarity and the flow field is consistent with theoretical plume scalings, showing a dependence on source buoyancy flux for predictions in this region. The extent of the transition region where plume self-similarity breaks down is defined, and its importance in the context of in-situ observations is highlighted. Finally, we show that extreme temperatures above 100°C occur in the first two meters of the column, but exposure times for a proxy tracer are short, suggesting that hydrothermal plumes could serve as viable transport vectors for biological materials.

## Plain Language Summary

Hydrothermal vent fields on the ocean floor release hot, mineral-rich water that forms rising plumes, known as black smokers. These plumes are critical to the unique ecosystems around vents (the source points) and influence how heat and materials spread through the ocean. However, the details of plume behavior near the seafloor, where they are most energetic, remain poorly understood. Using advanced computer simulations, we studied these plumes at high resolution, focusing on the region close to the vent. We examined how the plumes mix with the surrounding water and found that the mixing rate changes significantly with height and time. The results were compared with in-situ data and plume theory. Vent temperatures reach 300°C, but anything transported by the plumes would only experience these extreme conditions for very short times. This suggests that hydrothermal plumes may carry biological material, such as larvae, without causing harm. We also studied how vent conditions affect plume behavior, focusing on its transition from the source-dominated region to the turbulent region farther away, where it aligns with the established theory. The transition zone shows behaviors crucial for interpreting seafloor observations. Our findings provide new insights into how hydrothermal plumes behave and interact with deep-sea environments.

## 1 Introduction

Unlike most of the abyssal plain, hydrothermal fields are oases of life and sites of complex chemistry (Van Dover, 2002; Cotte et al., 2020), where hot fluids are discharged through vents from chimney structures as black smokers, i.e., buoyant plumes. While the total Earth’s surface heat flux is typically  $\mathcal{O}(0.1 \text{ W m}^{-2})$  (Sclater et al., 1980; Davies & Davies, 2010), hydrothermal plumes can generate heat fluxes of up to  $\mathcal{O}(1 \text{ GW m}^{-2})$  (Mittelstaedt et al., 2012). They play a significant role in the heat flux balance of hydrothermal fields (Barreyre et al., 2012; Mittelstaedt et al., 2012), influence faunal assemblages several meters away from fluid discharge points (Girard et al., 2020), and contribute to the injection of dissolved iron and rare earth elements into the ocean (Chavagnac et al., 2018).

Hydrothermal plumes typically rise several hundred meters (Lavelle et al., 2013; Adams & Di Iorio, 2021) in the weakly stratified deep ocean, while vent radii are on the order of centimeters. The discharged fluids reach temperatures of  $\sim 400 \text{ }^\circ\text{C}$  and fluid

64 velocities of up to  $\sim 1 \text{ m s}^{-1}$ , e.g., Koschinsky et al. (2008); Sarrazin et al. (2009), mak-  
65 ing hydrothermal plumes an exotic phenomenon in contrast to typical ocean conditions.  
66 Vent characteristics give rise to a wide range of plume behaviors, from jet-like plumes  
67 (forced plumes) to highly buoyant plumes (lazy plumes). The great depths involved make  
68 in-situ observations challenging, with data collection generally limited to the first few  
69 meters above the source to attribute measurements to a specific vent cluster. Only re-  
70 cent developments in acoustic imaging have efficiently captured hydrothermal system prop-  
71 erties (Xu et al., 2013; Bemis et al., 2015).

72 Despite the importance of buoyant plumes in hydrothermal fields, few numerical  
73 studies achieve resolutions that capture the physical processes at the scale of individual  
74 vents. Most studies investigate plumes at much larger scales, assuming that the hot fluid  
75 has already mixed with the environment and approximating the merging of vent fields  
76 (Lavelle et al., 2013; Tao et al., 2013; Gao et al., 2019; Adams & Di Iorio, 2021). This  
77 is largely due to the computational cost of achieving vent-scale resolution. Jiang and Breier  
78 (2014), however, approached this level of detail using Reynolds-Averaged Navier-Stokes  
79 (RANS) simulations, and showed that near-vent dynamics involve complex mixing pro-  
80 cesses.

81 Morton et al. (1956) established a simplified theoretical model of plume dynam-  
82 ics that successfully describes convective plumes in many situations (Kaye, 2008; Woods,  
83 2010). The model parameterizes turbulence with the assumption that the entrainment  
84 of surrounding fluid in the plume is proportional to its axial velocity. Dimensionless stud-  
85 ies outside the hydrothermal regime, using Direct Numerical Simulation (DNS) by Plourde  
86 et al. (2008); Taub et al. (2015); Marjanovic et al. (2017) and Large Eddy Simulation  
87 (LES) by Devenish et al. (2010), have demonstrated that the classical assumptions of  
88 the theoretical model do not hold in the near-field. In particular, forced or lazy plumes  
89 with initial buoyancy transition to a purely buoyant – pure plume – regime (Van Reeuwijk  
90 & Craske, 2015). The adjustment between the near-field and far-field hinders the appli-  
91 cation of theoretical models (Ciriello & Hunt, 2020) and has been poorly characterized  
92 for plumes, with even less attention given to the hydrothermal regime.

93 The aim of this paper is therefore to work within a realistic framework, specifically  
94 in the hydrothermal regime. We focus on the near-vent region, which represents the win-  
95 dow for in-situ operations and where black smokers interact with biochemical processes.  
96 This makes the results directly applicable to the scale of hydrothermal fields.

97 In particular, due to their proximity to benthic communities, hydrothermal plumes  
98 may serve as a mechanism for the vertical transport of larvae (Kim et al., 1994; Mullineaux  
99 & France, 1995), influencing larval dispersal within the regional circulation (Xu et al.,  
100 2018; Vic et al., 2018). However, no studies have focused on the near-vent region at high  
101 resolution, particularly with regard to the influence of potentially lethal high temper-  
102 atures on biotracers. This work aims to quantify the exposure time to high temperatures  
103 in black smokers for a proxy tracer.

104 To address the near-vent physics of buoyant plumes with adequate resolution, we  
105 use a Large Eddy Simulation (LES) approach with adaptive mesh refinement, which al-  
106 lows centimeter-scale resolution within a 6 m domain above the vent. Specifically, we ex-  
107 tensively study conditions encountered at the Lucky Strike hydrothermal vent field (north-  
108 ern Mid-Atlantic Ridge), providing a realistic case study. This approach allows us to gain  
109 new insights into the near-field hydrothermal regime, establish links with theoretical mod-  
110 els, and explore the link between hydrothermal plumes and near-vent benthic commu-  
111 nities.

112 The paper is organized as follows. Section 2 presents the governing equations and  
113 details of the numerical experimental setup. Section 3 investigates the turbulent field of  
114 a typical black smoker through its flow structure and compares it with the theoretical

115 model of Morton et al. (1956) and in-situ measurements. Section 4 extends the results  
 116 to a wide range of source parameters to examine the flow field from forced to lazy plume.  
 117 Section 5 discusses the impact of the transition regime on in-situ observations and the  
 118 effect of temperature fluctuations on biotracer proxies. A summary of the results is given  
 119 in section 6.

## 120 2 Model and Numerics

### 121 2.1 Plume Theory

122 The theory established by Morton et al. (1956) describes an axisymmetric Boussi-  
 123 nesq plume with a radius  $r$  in a stratified fluid, with the assumption that the radial pro-  
 124 files of vertical velocity  $w$  and buoyancy  $b$  are similar at all heights. This model is here-  
 125 after referred to as the MTT model. This approach relies on a parameterization of mix-  
 126 ing, the entrainment rate  $\alpha$ , which relates  $w$  at each height to the radial velocity  $e$  of the  
 127 entrained water in the plume, such that  $\alpha = e/w$ .

128 The conservation of volume, momentum, and buoyancy flux, under these assump-  
 129 tions, yields the following equations:

$$\frac{d}{dz}(r^2 w) = 2\alpha r w, \quad (1a)$$

$$\frac{d}{dz}(r^2 w^2) = 2r^2 b, \quad (1b)$$

$$\frac{d}{dz}(r^2 w b) = 2r^2 w \frac{g}{\rho_r} \frac{\partial \rho_a}{\partial z}, \quad (1c)$$

130 where  $\rho_a$  represents the ambient fluid density,  $\rho_r$  is a reference density, and  $g$  is the grav-  
 131 itational acceleration.

132 From the solutions of equations 1, the neutral buoyancy level  $H_{nbl}$  and the max-  
 133 imum height due to momentum overshoot  $H_{top}$  can be estimated as follows (Devenish  
 134 et al., 2010):

$$H_{nbl} = 1.04 \alpha^{-1/2} B_0^{1/4} N^{-3/4}, \quad (2a)$$

$$H_{top} = 1.36 \alpha^{-1/2} B_0^{1/4} N^{-3/4}, \quad (2b)$$

135 where  $N$  is the buoyancy frequency, and  $B_0 = \pi r_0^2 w_0 b_0$  is the buoyancy flux at the source,  
 136 with  $z = 0$  denoted by the subscript 0. The momentum flux and vertical volume flow  
 137 are defined as  $M_0 = \pi r_0^2 w_0^2$  and  $Q_0 = \pi r_0^2 w_0$ , respectively.

138 In most cases, hydrothermal plumes carry momentum from the source, induced by  
 139 subseafloor pressure. Morton and Middleton (1973) introduced two dimensionless pa-  
 140 rameters to characterize the balance of forces, expressed as

$$\Gamma(z) = \frac{r(z)b(z)}{\alpha w(z)^2}, \quad (3a)$$

$$\Gamma(z)' = \frac{\alpha b(z)}{r(z)N^2}. \quad (3b)$$

141 At  $z = 0$ ,  $\Gamma_0$  and  $\Gamma_0'$  represent the plume source parameters. For  $\Gamma_0 < 1$  the plumes  
 142 are forced (relative excess of momentum), and for  $\Gamma_0 > 1$  the plumes are lazy (relative  
 143 excess of buoyancy). When  $\Gamma_0' \ll 1$ , the plume is rapidly balanced by the ambient strat-  
 144 ification. The a priori choice of  $\alpha$  affects the  $\Gamma_0$  level and plume classification near  $\Gamma_0 =$   
 145 1. Taub et al. (2015) noted that this dependence can cause inconsistencies between the-  
 146 ory and observations.

147 The value of  $\alpha$  remains a subject of debate. The generally accepted values are 0.12  
 148 for buoyant plumes and 0.076 for pure jets (Woods, 2010; Kaye, 2008; Van Reeuwijk &

149 Craske, 2015; Richardson & Hunt, 2022). However, recent studies show that  $\alpha$  can vary  
 150 greatly in the near-field (Van Reeuwijk et al., 2016; Marjanovic et al., 2017). We assume  
 151 a fixed value of  $\alpha = 0.12$  for application to equations 1, 2, and 3.

## 152 2.2 Basilisk

153 Basilisk (Popinet, 2013) is an Adaptive Mesh Refinement (AMR) code that uses  
 154 an octree structure to discretize the computational domain. This approach provides re-  
 155 fined resolution in regions with small-scale features, while coarsening the grid in quies-  
 156 cent areas. The dynamic refinement adapts the mesh on the fly, efficiently focusing com-  
 157 putational effort on turbulent regions, making it well suited for plume studies. We set  
 158 the resolution so that the maximum resolution is  $d_{max} = 2.49$  cm to spatially resolve  
 159 the vent outlet, while the minimum resolution is set to  $d_{min} = 20$  cm. The code uses  
 160 a LES approach with a second-order accurate finite-volume solver for the Navier-Stokes  
 161 equations (Popinet, 2003, 2009, 2015). The equations are solved using the Boussinesq  
 162 and incompressibility assumptions, expressed as

$$\frac{\partial \mathbf{u}}{\partial t} + \nabla \cdot (\mathbf{u} \otimes \mathbf{u}) = \frac{1}{\rho_r} (-\nabla p + \nabla \cdot \mathbf{T}) + b \nabla z, \quad (4a)$$

$$\nabla \cdot \mathbf{u} = 0, \quad (4b)$$

163 where  $\mathbf{u}$  is the filtered velocity and  $z$  is the height above the source. The buoyancy is  
 164 defined as  $b = -g(\rho(x, t) - \rho_r)/\rho_r$ , where  $\rho(x, t)$  is the density at position  $x$  and time  
 165  $t$ . The model pressure  $p$ , representing the deviation from the hydrostatic reference pres-  
 166 sure  $P$ , is computed using a multigrid Poisson solver. Temperature  $T$  is integrated as  
 167 a conservative tracer using the robust upwind advection scheme of Bell et al. (1989). Den-  
 168 sity is computed by an extension of the Equation Of State (EOS) beyond the oceanic  
 169 funnel, namely for  $T > 40$  °C (see below). The stress tensor  $\mathbf{T}$  accounts for unresolved  
 170 small-scale turbulence. The Vreman (2004) sub-grid scale model is used to compute the  
 171 local eddy viscosity. This model requires a coefficient  $c$ , set to  $3.6 \times 10^{-2}$ , to allow a fair  
 172 chance for turbulent shear flow. The turbulent Prandtl number is set to unity, which im-  
 173 plies equal heat diffusivity and viscosity.

174 The Boussinesq approximation may seem questionable due to the large tempera-  
 175 ture anomalies at the vent, where the source temperature in this study is typically around  
 176  $T_0 = 300$  °C ( $\rho_0 = 782$  kg m<sup>-3</sup>) and the ambient temperature is  $T_a = 4.6$  °C ( $\rho_a =$   
 177  $1035$  kg m<sup>-3</sup>). However, the plume mixes rapidly as it exits (see section 3). At 25 cm  
 178 above the source, the average temperature drops to  $T = 50$  °C ( $\rho = 1021$  kg m<sup>-3</sup>), cor-  
 179 responding to an average density fluctuation of 1.4 % with respect to the reference den-  
 180 sity. At  $z = 1$  m, the mean temperature is close to  $T = 10$  °C, corresponding to a fluc-  
 181 tuation of 1 %, and temperatures of  $T > 40$  °C ( $\rho < 1025$  kg m<sup>-3</sup>) make up only 40  
 182 % of the distribution (Figure 2-e). Furthermore, the buoyancy flux is preserved in this  
 183 approximation. Thus, the introduced error is not expected to have a significant effect  
 184 on our results.

## 185 2.3 Equation Of State

186 An accurate EOS is needed for the 4–300 °C temperature range, at the hydrostatic  
 187 pressure of our target site, which is  $P \sim 1700$  dbar. TEOS-10 (IOC et al., 2010) is the  
 188 standard for computing seawater thermodynamics but is only valid in the oceanic fun-  
 189 nel, i.e.  $T < 40$  °C at 2000 m (McDougall et al., 2003). We need to extend the EOS  
 190 for temperatures above this range. Previous work by Sun et al. (2008) established a set  
 191 of fitted polynomial equations in the 4–300 °C range by combining freshwater and sea-  
 192 water data. A more recent study by Safarov et al. (2009), based on in-situ measurements  
 193 at  $S_A = 35.17$  g kg<sup>-1</sup>, covers the entire 0–195 °C range up to 1400 dbar with improved  
 194 accuracy. Bischoff and Rosenbauer (1985) determined the EOS for  $S_A = 32.16$  g kg<sup>-1</sup>  
 195 for the 200–350 °C range and up to 1000 dbar. To simplify the model, and due to a lack

196 of sufficient data, we neglect the specific chemistry of black smokers and assume a uni-  
 197 form absolute salinity of  $S_A = 35.2 \text{ g kg}^{-1}$ . To develop a smooth EOS that closely matches  
 198 these published results, we developed a non-linear parametric fit covering the temper-  
 199 ature and pressure range 0–350 °C and 1500–1700 dbar, typical of the conditions at Lucky  
 200 Strike (Figure A1). To balance the salinity differences, the data from Sun et al. (2008)  
 201 and Bischoff and Rosenbauer (1985) are adjusted based on TEOS-10 at  $S_A = 35.2 \text{ g kg}^{-1}$ .  
 202 The corresponding correlation is given in Appendix A by equation A1.

## 203 2.4 Outlet Turbulence Parameterization

204 The discrete sources observed at Lucky Strike systematically exhibit turbulence at  
 205 the vent, which is expected due to the complex and irregular subsurface circulation that  
 206 hot fluids undergo before reaching the seafloor (Fontaine et al., 2014). However, with-  
 207 out numerical adjustments, the plume initially develops as a transitional laminar flow  
 208 (Figure 1-a) until it destabilizes into a turbulent plume. This is an unrealistic feature  
 209 that is corrected using the method of Plourde et al. (2008). To trigger turbulence in the  
 210 plume, a uniform discrete white noise is added to the vertical velocity at all outlet nodes  
 211 (Figure 1-b, experiment 1 in Table 1), such that  $w = w_0(1 + AW(t))$ , where  $W(t)$  is a  
 212 white noise signal, and  $A$  is the noise amplitude. This parameterization represents the  
 213 turbulence pre-existing in the flow prior to injection into the water column and fully ac-  
 214 counts for the turbulent state at the outlet. The calculations show that for disturbance  
 215 magnitudes  $A = [0-2]$ , the level of turbulence can be increased while keeping the plume  
 216 numerically stable. However, a burst of viscous dissipation  $\varepsilon_k$  in the first nodes above  
 217 the outlet limits the maximum energy that can be injected at the source. Therefore, we  
 218 choose the optimal value of  $A = 0.5$ , which allows turbulence to develop quickly after  
 219 the outlet while minimizing the burst in  $\varepsilon_k$ .

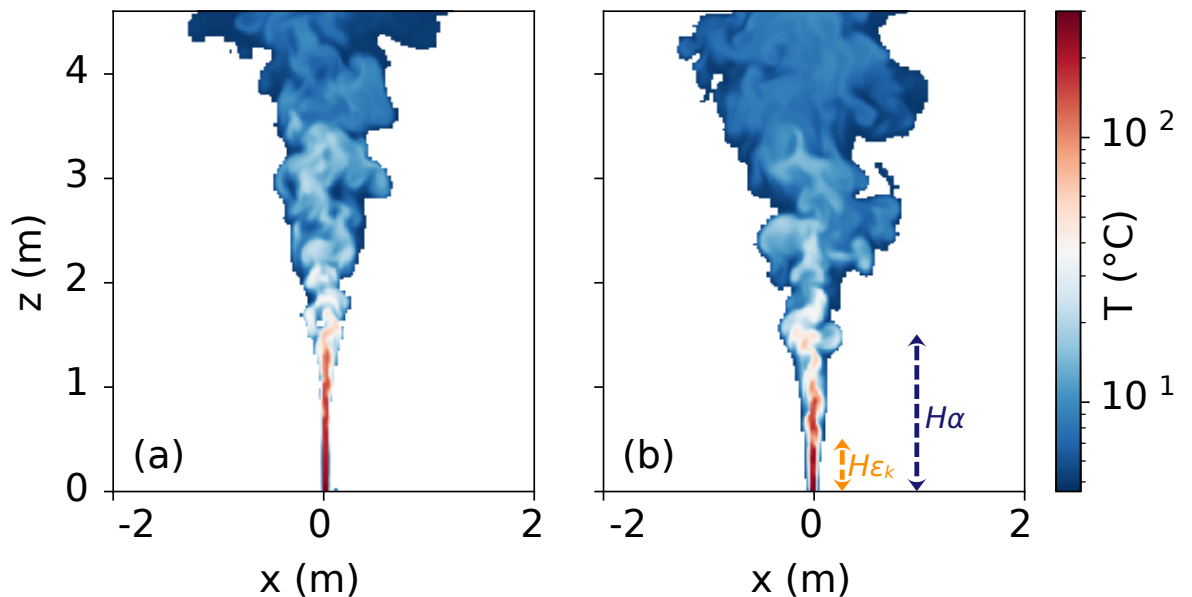


**Figure 1.** Cross-section of the instantaneous temperature field for (a) the scenario without noise perturbation at the outlet ( $A = 0$ ), and (b) with turbulence triggered by noise immediately after the outlet ( $A = 0.5$ ). The two reported heights correspond to the transition region to a pure plume regime (see section 4).

220

## 2.5 Experiment Setup and Modeling Case

221

222

223

224

225

226

227

The Tour Eiffel vent field (-1690 m) located at the Lucky Strike hydrothermal site (37°17'N 32°16'W) is selected as the baseline modeling case. It features a prominent 15 m high chimney with approximately 10 vents (Mittelstaedt et al., 2012) and is considered a biological hotspot (Van Audenhæge et al., 2022). We define a hydrothermal edifice as the collection of chimneys and complex topography resulting from hydrothermal activity. Usual structures are smaller than Tour Eiffel, typically  $\sim 1$ –2 m in height (Barreyre et al., 2014).

228

229

230

231

232

233

Hydrothermal fluid exits the seafloor through two types of sources: diffuse low temperature sources ( $T < 10$  °C), which are a mixture of hydrothermal fluid and ambient water, and discrete high temperature sources, typically black smokers (Barreyre et al., 2014). We focus on the plumes emitted by the latter. The EMSO-Açores (European Multidisciplinary Subsea Observatory) long-term observatory, maintained through the MoMARSAT campaign series, provides the framework for in-situ measurements.

234

235

236

237

238

239

240

241

242

243

The model domain is a cubic box of width  $L = 6.375$  m with open boundary conditions on all sides, except for a solid flat bottom. To avoid boundary effects, results are presented excluding regions near the boundaries. The plume is forced by imposing a temperature  $T_0$  and vertical velocity  $w_0$  at the vent, modeled as an outlet with radius  $r_0$ . A solid pipe was tested as a small chimney model to raise the outlet 1 meter above the seafloor to allow more effective entrainment of the surrounding fluid. Simulation results showed no significant differences, so for simplicity the outlet is kept at the bottom boundary. The ambient stratification is linear in the vertical, with  $N = 1.63 \times 10^{-3} \text{ s}^{-1}$ , determined from observations at Lucky Strike. The ambient temperature at the outlet is  $T_a = 4.6$  °C.

244

245

246

247

248

The diversity of source conditions is large, ranging from highly forced plumes to highly lazy plumes. To capture this variability, the study examines a number of key parameters:  $r_0$  (1.4–2.8 cm),  $w_0$  (0.02–1.4 m s<sup>-1</sup>), and  $T_0$  (40–340 °C). The selected range for these parameters is based on field data collected by Mittelstaedt et al. (2012) at Tour Eiffel. The experimental parameters are summarized in Table 1.

**Table 1.** Summary of simulations. The experiments are grouped based on common varying factors. The numerical domain size is  $L_0 = 6.375$  m. The maximum resolution is the same across all simulations ( $d_{max} = 2.49$  cm).

Experiment	Symbol	$w_0$ (m s <sup>-1</sup> )	$r_0$ (cm)	$T_0$ (°C)	$B_0$ (m <sup>4</sup> s <sup>-3</sup> )	$\Gamma_0$
1, 2, 3	■, ▲, ◆	0.7	2.8	[300, 100, 200]	[4.15e-3, 7.12e-4, 2.14e-3]	[1.1, 0.2, 0.6]
4, 5, 6	✦, ✧,	[1.4, 0.7, 0.4]	[1.4, 2.0, 2.8]	300	2.08e-3	[0.1, 0.8, 4.6]
7, 8	×, ►	[1.4, 0.1]	2.8	300	[8.30e-3, 2.97e-4]	[0.3, 224]
9, 10, 11	★, ●, ◀	0.5	[1.4, 2.0, 2.8]	300	[7.41e-4, 1.48e-3, 2.97e-3]	[1.1, 1.6, 2.2]
12, 13	◆, ●	[0.05, 0.2]	1.4	300	[7.41e-5, 2.97e-4]	[112, 7.0]
14, 15	▲, ●	[0.05, 1.4]	2.8	40	[1.13e-5, 3.16e-4]	[8.5, 0.01]
16, 17	→, ★	[0.05, 1.12]	[1.4, 2.8]	200	[3.82e-5, 3.42e-3]	[58, 0.23]
18	▼	0.02	2.8	340	1.61e-4	1897

249

## 2.6 Averaged Diagnostics

250

251

To synthesize the LES results, diagnostic quantities are averaged both in time and horizontally to provide vertical profiles. Horizontal averaging is performed within the plume,

252 which requires the definition of the plume boundary relative to the ambient. This def-  
 253 inition is not straightforward and there is no generally accepted approach in the liter-  
 254 ature. Few attempts have been made to provide a precise definition (Pham et al., 2005;  
 255 Plourde et al., 2008).

256 In this study, we define the plume boundary based on  $w$ : the plume interior is where  
 257  $|w| > \sigma$ . The typical value used is  $\sigma = 10^{-2} \text{ m s}^{-1}$ , determined by sensitivity tests,  
 258 with any deviations specified. This criterion filters velocities between 1% and 10% of the  
 259 axial values and is consistent with Morton et al. (1956)'s definition of the theoretical plume  
 260 radius. We have verified that this criterion accurately captures the plume boundary for  
 261 all source parameters in this study.

262 We define  $r(z, t)$  as the equivalent radius of the area  $S(z, t)$ , where  $S(z, t)$  is the  
 263 plume cross-sectional area used for horizontal averaging. On average,  $S(z, t)$  corresponds  
 264 to a disc, but this is not true for snapshot times, as turbulence causes the plume bound-  
 265 ary to become convoluted. The profiles are time-averaged over the integration time ( $\sim 10$   
 266 min plume time) with an output every 1.5 s.

267 The entrainment rate is a key quantity from the LES and is obtained by  $\alpha(z, t) =$   
 268  $e(z, t)/w(z, t)$ , where  $e(z, t)$  is the lateral flux entering the plume and  $w(z, t)$  is the mean  
 269 vertical velocity. It is computed using

$$e(z, t) = \frac{1}{2\pi r(z, t)} \frac{d}{dz}(wS), \quad (5a)$$

$$w(z, t) = \frac{1}{S(z, t)} \int_{S(z, t)} w dS. \quad (5b)$$

### 270 3 Model Result for a Black Smoker

271 The aim of this section is to describe the near-field plume dynamics, to investigate  
 272 the flow structure as a function of the entrainment rate, and to compare these results  
 273 with those predicted by the MTT theoretical model and in-situ data.

#### 274 3.1 Mean Field

275 The experiment presented here represents a typical source at the Lucky Strike field  
 276 (experiment 1 of Table 1). The regime is weakly lazy ( $\Gamma_0 = 1.14$ ), and as noted in sec-  
 277 tion 2.1, the choice of  $\alpha$  affects the value of  $\Gamma_0$ . Its turbulent flow is more similar to a  
 278 forced plume regime (see section 3.3), and the term forced plume is used for Experiment  
 279 1. We present the mean quantities averaged with  $\sigma = 1 \text{ cm s}^{-1}$  in Figure 2, together  
 280 with the 95th percentile mean to highlight the upper range of the data distribution. Pos-  
 281 itive and negative spatial standard deviations are shown separately.

282 The high value of  $\Gamma'_0 = 4 \times 10^6$  reflects the strong injection of  $B_0$  into a weak strat-  
 283 ification. The plume exits with an extremely high temperature anomaly ( $T - T_a \approx 300$   
 284  $^\circ\text{C}$ ) and intense momentum forcing ( $w_0^2 = 0.5 \text{ m}^2 \text{ s}^{-2}$ ), significantly different from typ-  
 285 ical ocean conditions. It results in  $H_{nbl} \approx 3400 r_0$  according to the MTT model (see  
 286 below), underscoring the focus on near-field behavior within this study ( $L_0 \approx 230 r_0$ ).  
 287 However, the plume quickly converges to a more tempered state within the numerical  
 288 domain, typical of the scale of hydrothermal edifices.

289 The mean temperature drops sharply from  $T_0 = 300 \text{ }^\circ\text{C}$  at the vent to less than  
 290  $T = 6.5 \text{ }^\circ\text{C}$  at  $z = 4 \text{ m}$ , and then follows a slower decay rate (Figure 2-b). Within the  
 291 first meter, the temperature drops below  $T = 15 \text{ }^\circ\text{C}$ . Despite this rapid decrease, the  
 292 region near the vent retains significantly high mean temperatures. The mean vertical ve-  
 293 locity goes from  $w_0 = 70 \text{ cm s}^{-1}$  to  $w = 7 \text{ cm s}^{-1}$  within the first meter (Figure 2-c).  
 294  $w$  remains almost constant above this, with only a 10% variation between  $z = 1 \text{ m}$  and



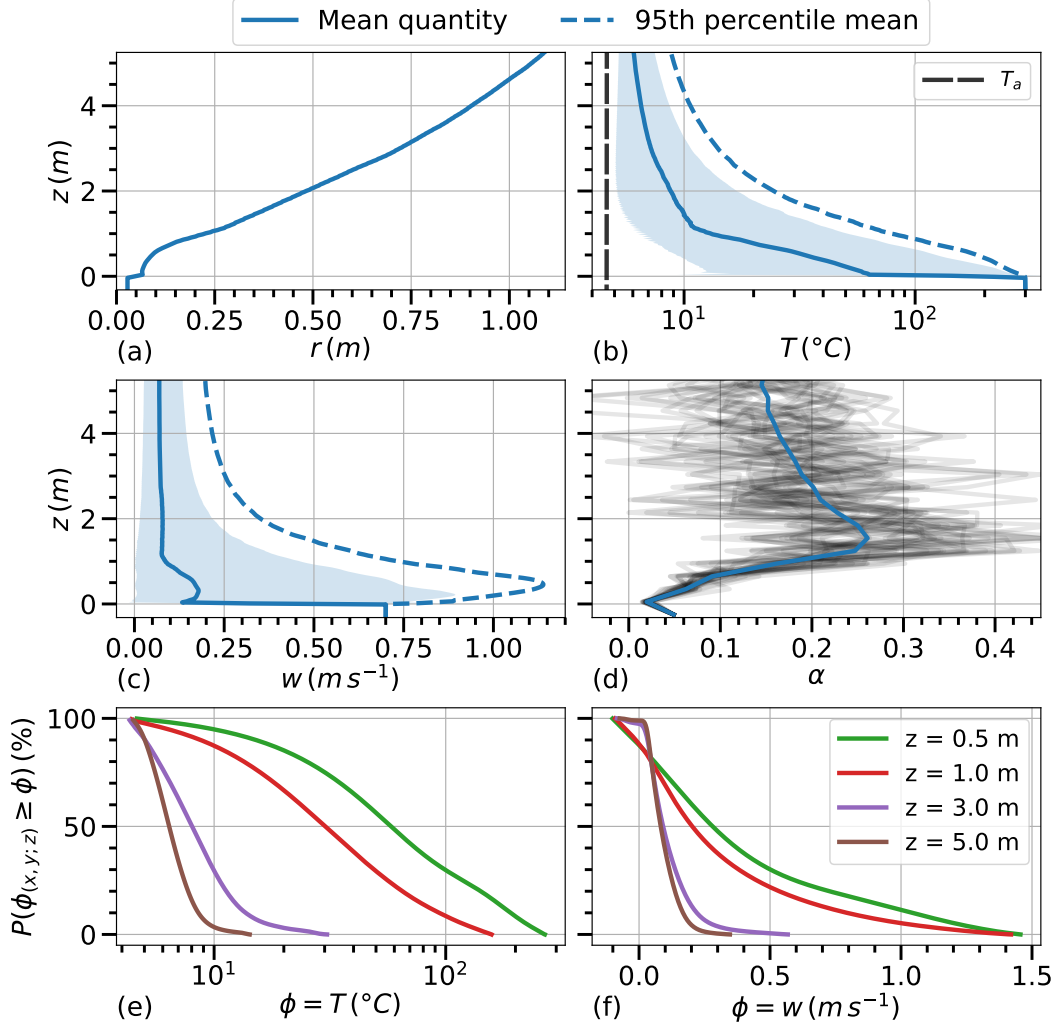


**Figure 2.** Vertical profiles for the time averaged (a) radius, (b) temperature, and (c) vertical velocity. (b)  $T_a$  is the ambient temperature (4.6  $^{\circ}\text{C}$ ). The dashed line represents the 95th percentile mean (core plume), and the shaded region indicates the asymmetric spatial standard deviation. (d) Evolution of the entrainment rate  $\alpha(z)$  and its temporal variability. Complementary cumulative density function for (e) temperature and (f) vertical velocity at different heights above the source.

295  $z = 5$  m. The first meter is characterized by fluid acceleration, with the plume core reach-  
 296 ing a peak velocity of  $w = 1.14$  m s<sup>-1</sup> at  $z = 0.5$  m, as discussed further below. The  
 297 radius increases linearly, indicating a constant spreading rate, reaching  $r = 1.05$  m at  
 298  $z = 5$  m. The area of averaging includes the boundary of the plume where most of the  
 299 mixing occurs. The averages are therefore sensitive to these regions of very low values,  
 300 which contribute to the sharp decreases in key variables and the rapid expansion observed  
 301 immediately after the outlet in Figure 2-a.

302 The plume dynamics observed in Figure 2, notably the stabilization of  $T$  and  $w$  pro-  
 303 files to nearly constant values, represent the adjustment between the near-field and far-  
 304 field regions. The entrainment of ambient water is necessary to dissipate the large val-  
 305 ues of  $T_0$  and  $w_0$  through mixing. This is reflected in the rapid increase in radius, which  
 306 grows by a factor of 37 between the vent and a height of  $z = 5$  m. This can be consid-  
 307 ered the dilution factor of the hydrothermal fluid (Figure 2-a). Coupled with the ver-  
 308 tical velocity, this results in a significant volume flow of  $Q = 0.25$  m<sup>3</sup> s<sup>-1</sup> at  $z = 5$  m.  
 309 Thus,  $Q$  grows by a factor of 145 over a height of  $z \approx 200 r_0$ , highlighting the efficiency  
 310 of buoyancy-driven entrainment.

311 The weak stratification has no significant effect in the near-field. It was included  
 312 in the LES setup to make the simulation more realistic and to avoid unnecessary assump-  
 313 tions about the surrounding fluid. However, LES runs under the same conditions as Ex-  
 314 periment 1, but with a uniform ambient, give identical results for the vertical profiles of  
 315 the mean quantities. Nevertheless, the parameter  $N$  is crucial for explaining the plume  
 316 equilibrium level and cannot be ignored in larger numerical domains. According to the  
 317 MTT model, the neutral buoyancy level and maximum height are predicted to be  $H_{nbl} =$   
 318 94 m and  $H_{top} = 123$  m, respectively (equations 2-a, b). The solution of the MTT equa-  
 319 tions in uniform versus stratified environments begins to diverge at  $z \approx 0.4H_{nbl}$ . Here,  
 320 the numerical domain represents  $0.07H_{nbl}$ , which seems to be a reasonable limit for as-  
 321 suming a uniform environment, without accumulating significant errors.

### 322 3.2 Spatial Fluctuations

323 The rapid drop in mean temperature does not mean that the hot water is imme-  
 324 diately and completely mixed. Mixing takes some time. The 95th percentile distribu-  
 325 tion is assumed to represent the core of the plume. In this region, the temperature is sig-  
 326 nificantly higher than at the plume's edge (Figure 2-b), where ambient cold water is drawn  
 327 in and subsequently mixed.

328 To understand the mixing process, we present the Complementary Cumulative Den-  
 329 sity Function (CCDF) for temperature at different heights above the source (Figure 2-  
 330 e). The CCDF shows the probability of finding a parcel at height  $z$  with a temperature  
 331 greater than  $T$ . For example, at  $z = 1$  m, 50 % of the parcels have temperatures above  
 332 30 °C, and 10 % exceed 100 °C, while the mean temperature is only 10 °C. This provides  
 333 information beyond the predictions of the MTT model and is valuable for understand-  
 334 ing chemical processes and larval dispersal. Implications for biological particles are dis-  
 335 cussed in section 5.2. At  $z = 3$  m, the maximum observed temperature is 30 °C.

336 We apply the same diagnostic to the vertical velocity (Figure 2-f). Two points stand  
 337 out. First, local velocities can reach up to twice the exit velocity (up to 1.5 m s<sup>-1</sup>) be-  
 338 low  $z = 1$  m. Second, downward velocities occur within the plume, although with low  
 339 probability. The latter is directly related to the twisting vortical structures and their as-  
 340 sociated circulations (Figure 3). The first property shows that the core of the plume is  
 341 being accelerated. This acceleration is driven by buoyancy, with the available potential  
 342 energy carried by the hot water acting as a source of kinetic energy (Winters et al., 1995;  
 343 Wykes et al., 2015). Figure 2-c clearly shows that the vent buoyancy provides a local  
 344 acceleration of the core plume, strong enough to influence the mean value. The fluid ac-  
 345 celeration means that any in-situ measurement must take this effect into account, as es-

346 timating the vent volume flow just centimeters above the source could lead to significant  
 347 errors.

348 The distribution of large anomalies in  $T$  and  $w$  remains significant within the first  
 349 meter. Due to the high temperature of the core being mixed, a specific extension of the  
 350 TEOS-10 EOS is still required 1 m above the vent. This highlights that the assumption  
 351 of a homogenized fluid based on mean quantities, with low  $w$  and  $T$  values for  $z < 3$   
 352 m, is incorrect. However, mixing drastically changes the balance of forces, subsequently  
 353 slowing the vertical motion and reducing the variance in the plume quantities  $w$  and  $T$ .  
 354 Beyond this region ( $z > 3$  m) the distributions of  $T$  and  $w$  show reduced spatial vari-  
 355 ation, which explains the slower decrease of their profiles and their convergence to nearly  
 356 constant values. At  $z = 5$  m, the absolute spread of  $T$  and  $w$  decreases to 10 °C and  
 357 0.34 m s<sup>-1</sup>, with a lower probability of extreme values, compared to an absolute spread  
 358 of 155 °C and 1.4 m s<sup>-1</sup> at  $z = 1$  m.

359 A key result is that the flow structure must be carefully considered in experiments  
 360 that initiate simulations at a dilute point above the vent, as many hydrothermal plume  
 361 simulations rely on this approach (Lavelle et al., 2013; Gao et al., 2019; Adams & Di Io-  
 362 rio, 2021). Approximating a uniform source below  $z = 5$  m fails to capture the dynam-  
 363 ics of the near-vent flow structure. In particular, the velocity fluctuations indicate that  
 364 turbulence is fully developed, and the plume cannot be assumed to be laminar in the near-  
 365 field.

### 366 3.3 Entrainment and Flow Structure

367 The entrainment rate,  $\alpha(z, t)$ , shows strong vertical and temporal variability, as-  
 368 sociated with intense mixing and the plume dilution. The overall value in the domain  
 369 is  $\alpha = 0.19$ , but it shows a vertical dependence with three distinct zones, consistent with  
 370 previous results obtained using DNS by Van Reeuwijk et al. (2016). For  $z < 0.7$  m, the  
 371 forced plume is driven by the source condition. The entrainment rate is similar to that  
 372 of a jet-like plume,  $\alpha = 0.07$ . This region corresponds to most in-situ observation ca-  
 373 pabilities. Between 1 m  $< z < 2$  m, the entrainment rate reaches its maximum ( $\alpha =$   
 374 0.26), which is twice the commonly accepted value for buoyant plumes. This entrainment  
 375 rate reflects intense mixing with cold fluid, contributing to the plume spreading, as well  
 376 as the dilution and homogenization of the temperature anomaly distribution. Buoyancy  
 377 driving the flow weakens, resulting in deceleration. For  $z > 3$  m, the entrainment rate  
 378 converges to a more conventional value ( $\alpha = 0.15$ ) for a pure plume (Van Reeuwijk &  
 379 Craske, 2015; Richardson & Hunt, 2022). This suggests that the plume reaches a self-  
 380 similar state, marking the end of the near-field transition regime (discussed in more de-  
 381 tail in section 4). This transition, as previously noted, is associated with an abrupt change  
 382 in the key variables  $T$  and  $w$  for  $z > 2$  m, with both converging to a weaker vertical  
 383 decay rate (Figure 2-b, c). The dilution process is responsible for the dissipation of the  
 384 large buoyancy flux  $B_0$  at the source.

385 The  $\alpha(z)$  profile is closely related to the turbulence field, which consists of differ-  
 386 ent scales of coherent structures. These structures can be observed using the  $\lambda_2$  tech-  
 387 nique (Jeong & Hussain, 1995), as shown in Figure 3. A real-time sequence of the tur-  
 388 bulent field observed with this technique is provided by the authors (Lemaréchal et al.,  
 389 2024a). The jet-like entrainment rate close to the source ( $z < 0.7$  m) is associated with  
 390 an unstable shear layer that forms ring vortices along the plume axis, typical of jet-like  
 391 flow. As the entrainment rate increases with height ( $z < 1.5$  m), the flow field becomes  
 392 turbulent. The vortices destabilize and break down into a helical mode, as described by  
 393 Fiedler (1988). The large, well-organized vortex structures between 1 m and 2 m, pre-  
 394 dominantly aligned in the horizontal plane, entrain more fluid than the smaller, less or-  
 395 ganized vortices that appear further downstream. This explains the maximum value of  
 396  $\alpha(z)$  observed at this height. This marks the transition region, where both the kinetic

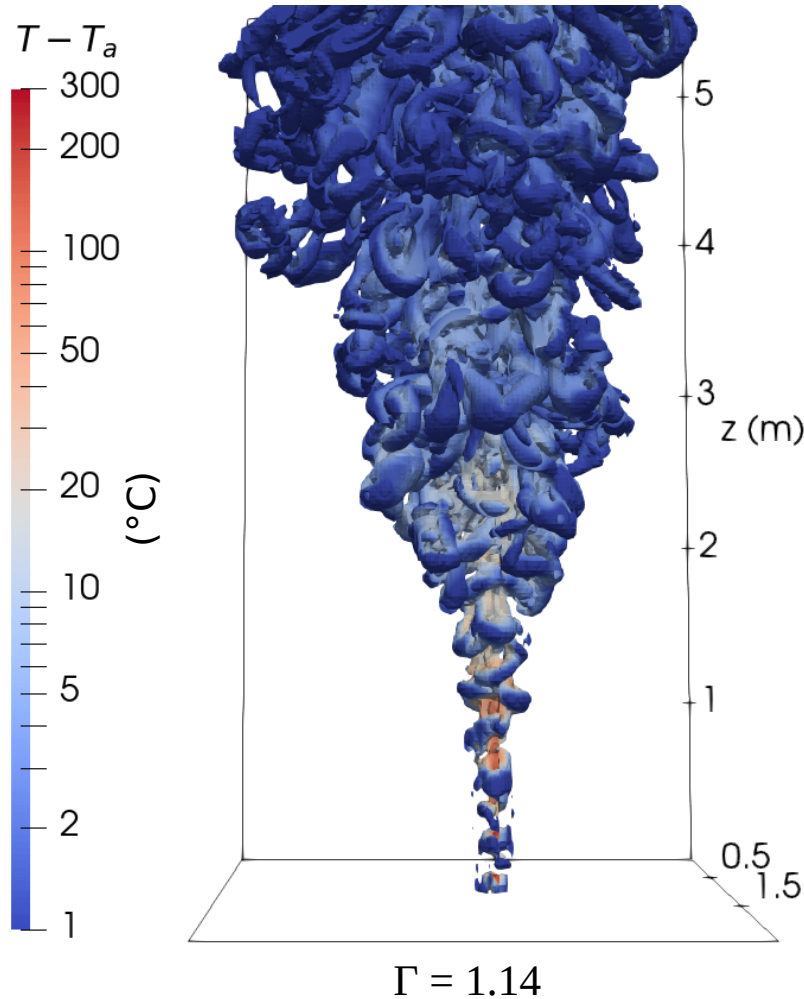


**Figure 3.** Three-dimensional coherent structures are visualized using the  $\lambda_2$  method (Jeong & Hussain, 1995) for iso-surfaces at  $\lambda_2 = -0.1$  for a plume near the forced plume regime (experiment 1). The colormap represents the temperature anomaly, with  $T_a = 4.6$  °C.

397 energy dissipation and the entrainment rate reach their peak. Beyond  $z = 1.5$  m, the  
 398 entrainment rate decreases as the flow enters a fully 3D convective turbulent state (pure  
 399 plume). The plume structure directly influences the entrainment rate and the energy dis-  
 400 sipation dynamics.

401 The instantaneous entrainment rate profiles (Figure 2-d – black lines) show signif-  
 402 icant temporal variability.  $\alpha(z, t)$  reaches a value of 0.5 at  $z = 1.6$  m, representing a  
 403 90% deviation from the mean. This observation adds to the evidence for strong mixing  
 404 in the vicinity of the vent. Similar behavior has been observed in experimental studies  
 405 (Matulka et al., 2014) and DNS studies (Plourde et al., 2008; Marjanovic et al., 2017).  
 406 We observe the same pattern in the hydrothermal regime. The temporal variability re-  
 407 sults from large-scale vortical structures driving the turbulent flow, as highlighted by Plourde  
 408 et al. (2008). Most of the entrainment occurs at the plume’s edge, while the core remains  
 409 less sensitive to mixing. Negative entrainment, up to  $\alpha = -0.06$ , is associated with de-  
 410 trainment processes reflected in the local downward velocities. This is associated with  
 411 the expulsion of fluid from the plume due to coherent turbulent structures. The influ-  
 412 ence of this mechanism on the mean field becomes noticeable only after  $z = 3$  m. Plourde

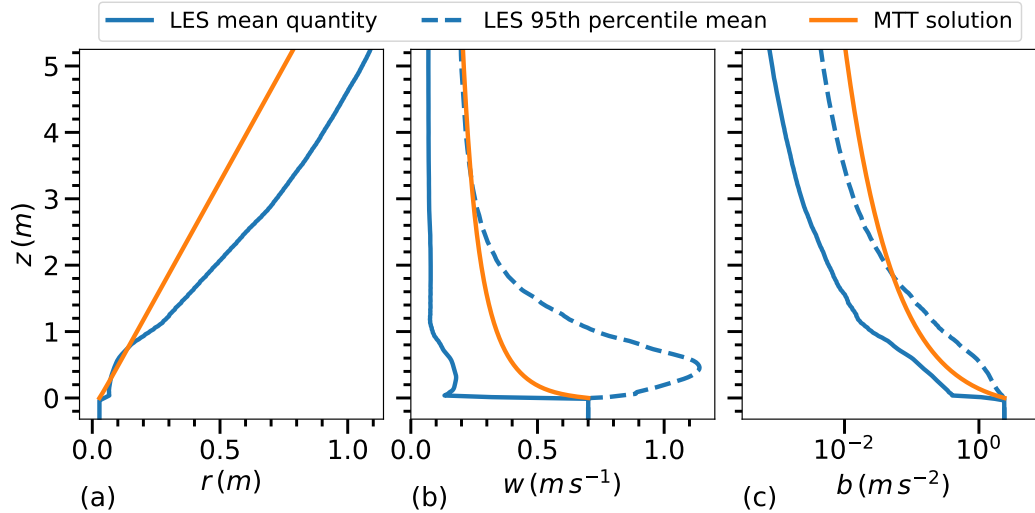


**Figure 4.** Vertical profiles of the flow field compared to the results obtained with the MTT model (1956) for its governing parameters: (a) radius, (b) vertical velocity, and (c) buoyancy. The dashed line represents the 95th percentile mean of the LES results (core plume).

413 et al. (2008), using higher resolution DNS, identified it as an expulsion and contraction  
 414 mechanism of local coherent structures driving the dominant entrainment process.

### 415 3.4 Comparison with the MTT Model

416 LES mean quantities can be compared with predictions from integral models. Figure  
 417 4 compares LES data with the MTT model predictions, the most widely used theo-  
 418 retical model. It shows that the self-similar conservation equations derived by Morton  
 419 et al. (1956) do not hold in the near-field. The MTT equations in Figure 4-a, b, c  
 420 capture the general trend of the flow field but do not agree well with the mean profiles. This  
 421 discrepancy cannot be attributed to horizontal averaging choices, as the MTT model best  
 422 represents the core plume evolution for  $z > 2$  m. At  $z = 5$  m, the radius predicted  
 423 by the MTT model is 30 % smaller, and the difference in the velocity profiles results in  
 424  $Q = 0.37 \text{ m}^3 \text{ s}^{-1}$ , which is 30 % higher than the LES flow field.

425 In particular, the fluid acceleration contradicts the self-similarity assumption in the  
 426 MTT model, which predicts a monotonic decrease in vertical flow velocity (Figure 4-b).  
 427 This was shown by Marjanovic et al. (2017) for lazy plumes. Here, we show that the buoy-  
 428 ancy flux injected by black smokers in a forced plume regime is sufficient to induce the  
 429 same effect.

430 A virtual origin correction can be applied to the source to account for the point  
 431 source assumption of the MTT model (Hunt & Kaye, 2001). However, the length  $L_q =$   
 432  $5Q_0/(6\alpha M_0^{1/2})$ , which represents the distance from the actual source to the virtual source  
 433 of a pure plume (Hunt & Kaye, 2005), has little effect on the results ( $L_q = 29$  cm) and  
 434 is therefore not applied.

435 The adjustment between the vent conditions and an ordered far-field flow, corre-  
 436 sponding to a pure plume regime, is responsible for the breakdown of the self-similarity  
 437 assumption. This prevents the direct application of the theoretical model. This is in agree-  
 438 ment with recent findings by Matulka et al. (2014); Van Reeuwijk et al. (2016); Marjanovic  
 439 et al. (2017); Ciriello and Hunt (2020) and highlights the need for analytical solutions

440 adapted to this region. This adjustment to the far-field occurs through mixing, which  
 441 is reflected in the strong variability of the  $\alpha(z, t)$  profile. Thus, our work confirms the  
 442 main limitation of the MTT model: the entrainment rate cannot be assumed constant  
 443 in the transition region between the near-field and far-field. It shows that although the-  
 444 theoretical models are often used to calibrate measurement techniques (Crone et al., 2008;  
 445 Mittelstaedt et al., 2012), near-field hydrothermal plume predictions cannot rely solely  
 446 on these models.

447 Another approach to measuring the entrainment rate is to derive  $\alpha$  from the spread-  
 448 ing rate, represented by the local derivative  $\partial z/\partial r$  and expressed as the angle  $\hat{\beta}$  between  
 449 the plume boundary and the horizontal. Plumes do not always maintain a constant spread-  
 450 ing rate, particularly in cases of necking in lazy plumes (Marjanovic et al., 2017). Here,  
 451 however, the radius shows a steady increase, corresponding to a nearly constant angle  
 452  $\hat{\beta} = 84^\circ$ . The spreading rate is linked to the MTT assumptions through  $\alpha$ . Applying  
 453  $\hat{\beta}$  to the conservation of volume in the MTT model gives a theoretical value of  $\alpha = 0.10$ .

454 Two key points can be made. First, the spreading rate remains nearly constant in  
 455 the near-field for hydrothermal plumes. This is consistent with the assumption of the  
 456 model developed by Priestley and Ball (1955), which is related to the MTT model (Fox,  
 457 1970). Secondly, the derived value of  $\alpha = 0.10$  is close to the classical one (Richardson  
 458 & Hunt, 2022), while the mean value  $\alpha = 0.19$ , obtained through direct computation,  
 459 is almost twice as high due to the turbulent field in the near-vent region. This shows that  
 460 while black smokers can be captured to some extent by integral models, these models  
 461 fail to reproduce the detailed dynamics observed near the vent.

### 462 3.5 Comparison to In-Situ Observations

463 Here, we assess how accurate our model is compared to direct measurements. Re-  
 464 producing black smokers in laboratory experiments is technically challenging (Shabbir  
 465 & George, 1994; Crone et al., 2008), while accessing hydrothermal fields at depth presents  
 466 its own set of challenges. Our LES results are compared with in-situ data from the Mo-  
 467 MARSAT2023 cruise using Remotely Operated Vehicle (ROV) operations.

468 The in-situ experimental setup is shown in Figure 5. Sampling was performed at  
 469 a typical source in the Tour Eiffel field. The vertical observation window,  $H_{obs}$ , is lim-  
 470 ited to 60 cm above the vent. The key parameters to be retrieved are the plume radius  
 471 and the temperature profile. The optical width, i.e., the visible gradient density anom-  
 472 alies, provides a measure of the apparent radius of the plume, although this measure is  
 473 subject to perspective distortion. Radius measurements are based on video recordings  
 474 with a reference scale, consisting of 300 frames and a step size of  $dz_{obs} \approx 5\% H_{obs}$ . The  
 475 temperature profile is measured with a probe positioned along the plume centerline above  
 476 the vent, with  $dz_{obs} \approx 10\% H_{obs}$  and a sampling rate of 1 Hz. Horizontal currents were  
 477 negligible during the experiment.

478 The in-situ data are compared with the LES equivalent in Figure 6 (experiment  
 479 9 of Table 1). The values of  $r_0 = 1.4$  cm and  $T_0 = 300$  °C for the LES experiment are  
 480 chosen based on the in-situ measurements at  $z = 0$  m. The Root Mean Squared (RMS)  
 481 value is used to represent the temporal dispersion of the in-situ data.

482 The vertical velocity at the source is a complicated parameter to measure accurately  
 483 using only video data (Crone et al., 2008; Mittelstaedt et al., 2012). First,  $\sigma$  is set to 10  
 484 cm s<sup>-1</sup>, which captures the plume contour effectively measurable in videos. For any given  
 485 set of source parameters tested, a smaller  $\sigma$  value includes density gradients too weak  
 486 to be detected visually in the video, as well as colder parcels. This causes an incoher-  
 487 ent sharp increase and decrease in  $r$  and  $T$ , respectively, immediately after the exit (Fig-  
 488 ure 6-a, b). Then,  $w_0$  is estimated based on LES experiments. Several experiments are  
 489 run with the same  $r_0$  and  $T_0$  values as above, to determine the  $w_0$  value that gives a ra-

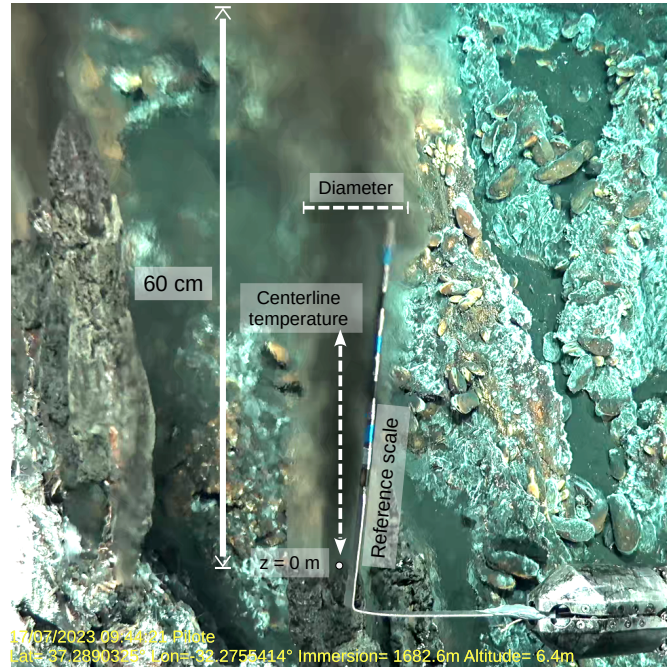


**Figure 5.** Photograph of the plume and schematic of the parameters used to measure the temperature and diameter of the plume. The reference scale gives the pixel-to-real distance ratio. Height above the source is measured from the reference point at  $z = 0$  m. Diameter is measured by identifying the visible outer edges of the plume relative to the surroundings. Temperature is measured along the centerline of the plume.

490 dius and temperature profile that best matches the in-situ data. It is found to be  $w_0 =$   
 491  $0.5 \text{ m s}^{-1}$ .

492 The LES radius and temperature profiles are in good agreement with the exper-  
 493 imental data. The variability of the in-situ radius at  $z_0$  reflects the temporal evolution  
 494 of the effective equivalent surface through which the flow passes. In fact, the vent ge-  
 495 ometry does not resemble a well-defined pipe, but consists of closely spaced sources, each  
 496 less than a centimeter wide, which together form a single plume exit. The RMS of the  
 497 in-situ data increases with height as the plume moves and bends away from its axis, in-  
 498 troducing a bias from the 2D view of the apparent radius, which is not captured by the  
 499 LES method of calculating  $r$ .

500 The LES plume is slightly colder at the source, but this does not significantly af-  
 501 fect the profiles. The LES experiment accurately reproduces the rapid decrease from  $220$   
 502  $^{\circ}\text{C}$  at  $z = 5 \text{ cm}$  to  $85 \text{ }^{\circ}\text{C}$  at  $z = 30 \text{ cm}$ . The blue dots in Figure 6-b represent the pro-  
 503 file expected from LES for a thermal sensor placed on the axis. Due to the stirring ef-  
 504 fect of turbulent structures, the mean profile along the axis is interchangeable with the  
 505 temperature averaged over a slice bounded by  $\sigma = 50 \text{ cm s}^{-1}$ . This indicates that  $w$   
 506 measurements on the axis are expected to be larger than this  $\sigma$  value.

507 The in-situ profile deviates from the LES profile for two reasons. In practice, the  
 508 sensor is not perfectly centered, resulting in a colder in-situ profile. The in-situ profiles  
 509 correspond better to the mean LES profile for the area bounded by  $\sigma = 10 \text{ cm s}^{-1}$ . Sec-  
 510 ond, the thermal inertia of the instrument misses the parcels with the highest fluid tem-  
 511 peratures, such as rapidly ascending turbulent structures, as shown by the small RMS  
 512 of the field data compared to the LES spatial variability.

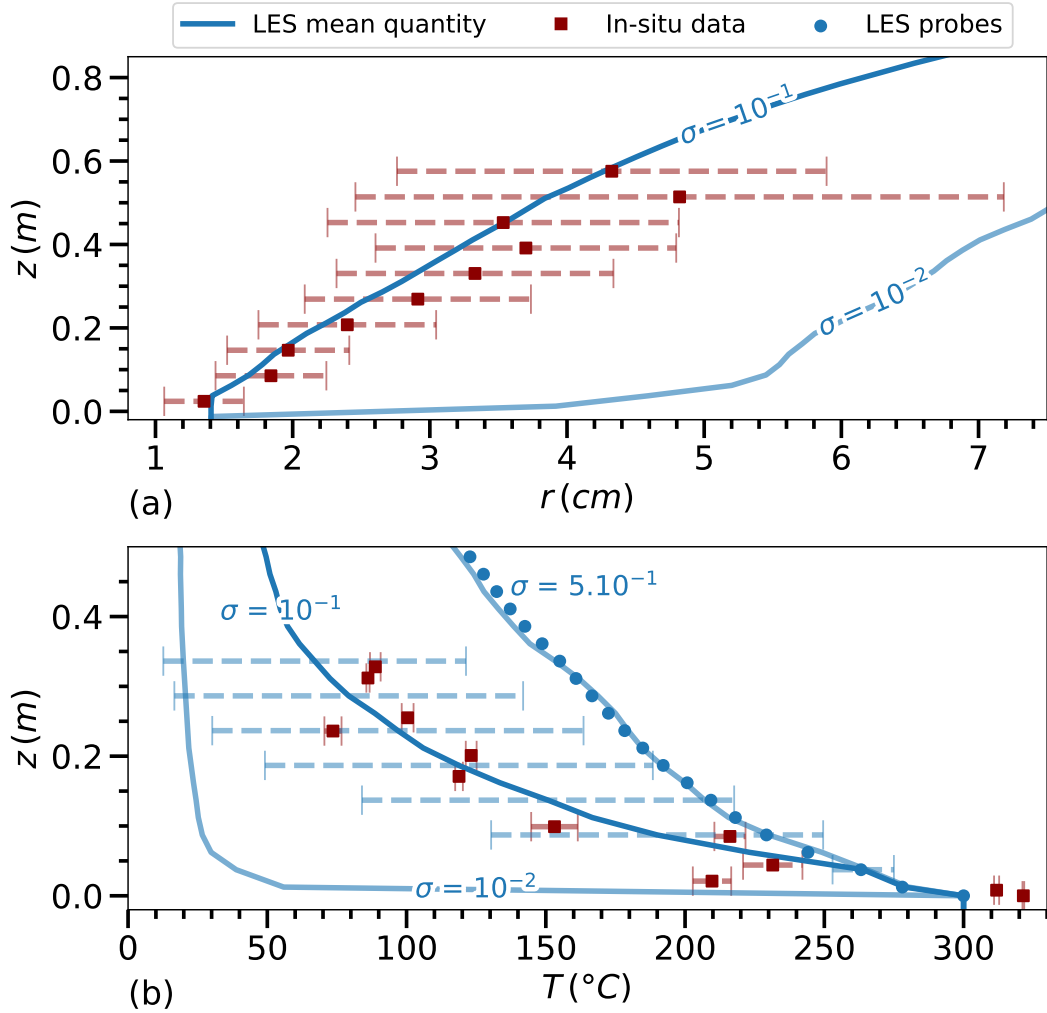


**Figure 6.** Profiles of (a) the plume radius and (b) temperature for the in-situ data and the LES mean quantities for different values of  $\sigma$  (in  $\text{m s}^{-1}$ ). The blue dots represent numerical probes indicating the time-averaged temperature at the plume axis. The error bars represent the spatial RMS for the LES data and the temporal RMS for the in-situ data.



513 The consistency of the LES and in-situ radius and temperature profiles for  $H_{obs} =$   
 514 60 cm gives us confidence in the reliability of the LES model in the near-vent region, in  
 515 contrast to the MTT model. In addition, the good agreement close to the source vali-  
 516 dates the parameterization of the vent turbulence.

## 517 4 Sensitivity to Source Parameters

518 Hydrothermal plumes can exist under a wide range of conditions, from forced to  
 519 lazy plume regimes. In this section, we extend the results to a large set of vent source  
 520 parameters. We provide a detailed description of the transition region from the near-vent  
 521 to the pure plume regime. The resulting flow field adjustments are analyzed on the ba-  
 522 sis of plume theory. We use experiments 1 to 18 (Table 1), for which the set of condi-  
 523 tions is summarized in Figure 7-a, covering most of the parameter space of hydrother-  
 524 mal vents.

### 525 4.1 Transition Region

526 As the plume mixes with the ambient fluid, the potential energy of the density anomaly  
 527 decreases, and a fraction of it is converted into momentum through the buoyancy flux  
 528 (Wykes et al., 2015). Therefore, assessing the transition height  $H_t$  based on the ratio of  
 529 forces using the  $\Gamma(z)$  parameter becomes complicated because the momentum combines  
 530 with the kinetic energy resulting from buoyancy. Indeed, several studies have shown that  
 531  $\Gamma(z)$  exhibits complex behavior before converging to 1 (Hargreaves et al., 2012; Taub et  
 532 al., 2015; Marjanovic et al., 2017), and its dependence on  $\alpha$  further complicates the task.

533 To address this issue, we frame the transition region using two indicative heights.  
 534 The first height,  $H_{\varepsilon_k}$ , corresponds to the location of maximum viscous dissipation, ex-  
 535 cluding the peak associated with noise injection. A consistent pattern in the vertical pro-  
 536 file of viscous dissipation is observed across all results, showing an increase that culmi-  
 537 nates in a peak within the first meter. This point indicates the establishment of a bal-  
 538 ance between the shear generated by the injection of momentum and the buoyancy force.  
 539 The second height,  $H_\alpha$ , marks the location where the maximum entrainment of ambi-  
 540 ent water occurs, indicating the complete destabilization of the plume column into 3D  
 541 turbulence. As noted by Taub et al. (2015); Marjanovic et al. (2017),  $\alpha(z)$  converges to  
 542 a constant in the self-similar state. These heights are illustrated in Figure 1-b.

543 Figure 7-b shows the rapid horizontal expansion in the transition region for a highly  
 544 lazy plume (S1 - experiment 12), a plume in balance (S2 - experiment 9), and a forced  
 545 plume (S3 - experiment 7).  $H_{\varepsilon_k}$  and  $H_\alpha$  effectively capture the transition from vertical  
 546 streamlines to a turbulent field (Figure 3) and frame the maximum of the derivative  $d \log(r^2/r_*^2)/dz$ ,  
 547 where  $r_*$  is a reference radius. In Figure 7-c, the heights  $H_{\varepsilon_k}$  and  $H_\alpha$  are plotted against  
 548 the parameter  $\Gamma_0$ . Two key points emerge.

549 Despite a 6 order of magnitude variation in  $\Gamma_0$ , the transition region exhibits rel-  
 550 atively small amplitude changes ( $\Delta H_{\varepsilon_k} = 0.5$  m and  $\Delta H_\alpha = 0.95$  m). This shows that  
 551 the transition region remains almost invariant to the set of parameters  $r_0$ ,  $w_0$  and  $b_0$  en-  
 552 countered at the hydrothermal site.  $H_\alpha$  ranges from 1.20 m to 2.15 m, and  $H_{\varepsilon_k}$  ranges  
 553 from 0.25 m to 0.75 m, with S1 and S3 differing by a factor of only 1.7. However, a simi-  
 554 lar trend emerges for both heights  $H_{\varepsilon_k}$  and  $H_\alpha$ . The transition region extends further  
 555 away from the source as  $\Gamma_0$  increases. This is consistent with the results of Taub et al.  
 556 (2015), whose analysis of entrainment rate profiles suggests that lazy plumes reach self-  
 557 similarity further away from the source than forced plumes.

558 Forced plumes – up to  $\Gamma_0 = 1$  – driven by momentum flux are unstable, charac-  
 559 terized by intense shear leading to rapid destabilization of the column ( $H_{\varepsilon_k} \approx 0.3$  m  
 560 for  $\Gamma_0 < 1$ ). When the source buoyancy flux balances the input momentum, it slows

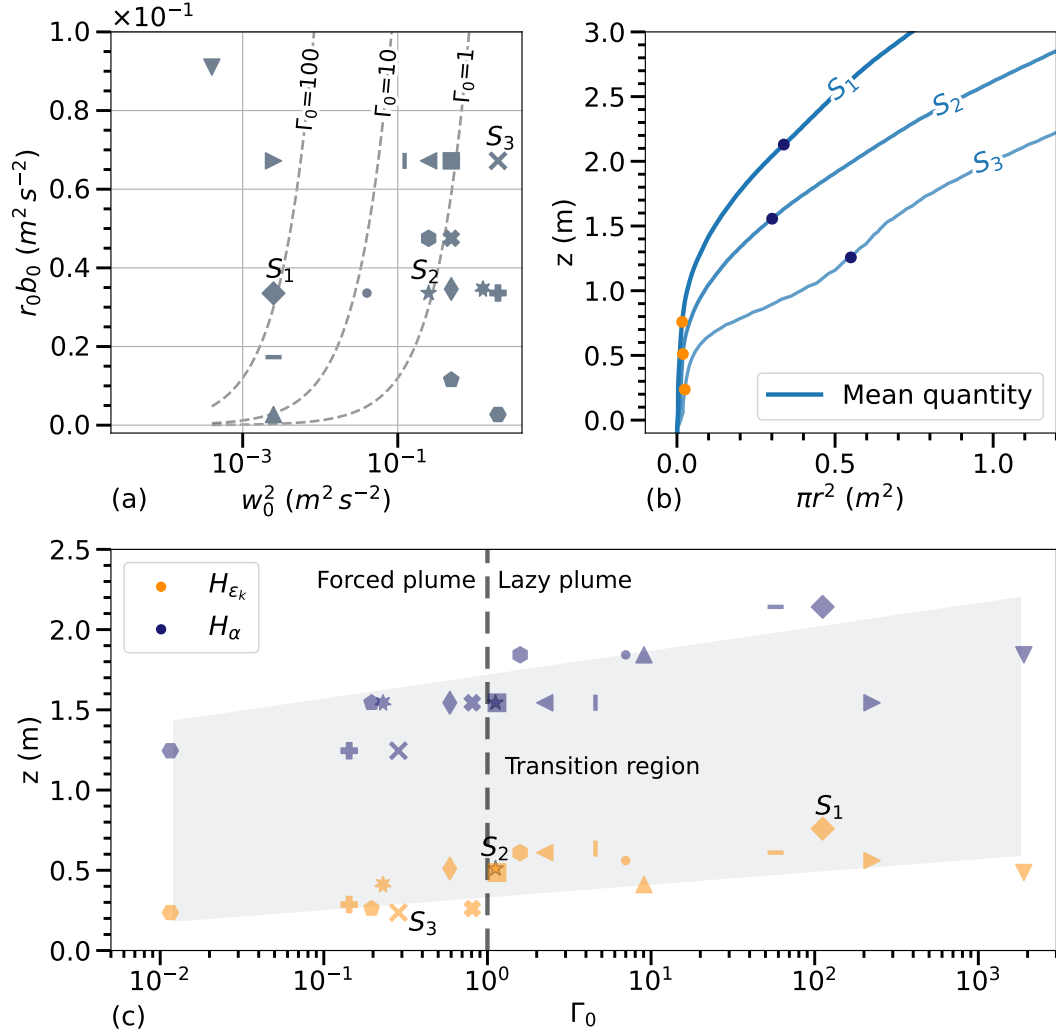


**Figure 7.** (a) Ratio of input buoyancy-radius product to momentum for experiments 1 to 18. (b) The surface of horizontal expansion for three different source conditions, with their transition heights defined by  $H_{\epsilon_k}$  (in orange) and  $H_\alpha$  (in blue). (c) Transition heights as a function of  $\Gamma_0$ , the plume source parameter. The dashed line separates the forced and lazy plume regimes, while the grey area encompasses the plume’s transitional state.

561 the development of convective turbulence compared to jet-like plumes ( $H_{\varepsilon_k} \approx 0.5$  m  
 562 for  $\Gamma_0 = 1$ ). In all cases, the flow requires a minimum height of  $H_\alpha \approx 1.2$  m to fully  
 563 develop convective turbulence, even under a highly forced plume regime. It is worth not-  
 564 ing that the noise injected at the source accelerates the onset of turbulence.

565 The second consequence is that the transition region is not sharply delineated, as  
 566 it extends between  $H_{\varepsilon_k}$  and  $H_\alpha$ . The characteristic length scale,  $L_m = M_0^{3/4} B_0^{-1/2}$ , has  
 567 been proposed for forced plumes as the separation between jet-like and plume-like re-  
 568 gions by Morton (1959). A similar length scale for lazy plumes, marking the transition  
 569 to pure plume behavior, is  $L_a = Q_0^{3/5} B_0^{-1/5}$  (Hunt & Kaye, 2005). Recent studies by  
 570 Taub et al. (2015) and Wang and Law (2002) report  $z > 5 L_m$  or  $z > 6 L_m$  as the tran-  
 571 sition limit between jet-like and plume-like regions. However, these lengths do not ac-  
 572 curately represent the hydrothermal plume flow field. For  $\Gamma_0 < 1$ ,  $L_m \approx 18$  cm, and  
 573 the transition to the plume-like region occurs for  $z > 8 L_m$ , which is slightly higher but  
 574 still within reasonable agreement with the literature. In contrast,  $L_m$  increases for highly  
 575 forced plumes, which is not consistent with the trend observed for the LES. For  $\Gamma_0 >$   
 576 1,  $L_a \approx 4$  cm, but convergence to self-similarity clearly occurs at  $z > 40 L_a$ .

577 The high buoyancy flux involved may explain the limited relevance of both  $L_m$  and  
 578  $L_a$ . Our results support the definition of a relatively broad transition region, bounded  
 579 by  $H_{\varepsilon_k}$  and  $H_\alpha$ , above which the plume reaches a pure plume regime and below which  
 580 the source conditions dominate. This region is highlighted in grey in Figure 7-c, span-  
 581 ning from 0.25 m to 2.15 m, and is characteristic of hydrothermal vent conditions. For  
 582 simplicity, this region is referred to as  $H_t$  hereafter. The transition region corresponds  
 583 to the scale of hydrothermal edifices and falls within the range accessible by in-situ ob-  
 584 servational techniques, indicating that hydrothermal plumes observed near the seafloor  
 585 are typically in a transitional state.

586 Finally, the minimal effect of  $b_0$  and  $w_0$  on  $H_t$  suggests that other factors play a  
 587 more significant role.  $H_t$  is closely related to the vertical extent of the plume, with re-  
 588 sults showing  $H_t \approx H_{nbl}/100$ . While variations in  $r_0$  were limited due to small vent sizes  
 589 and could influence  $H_t$ , the parameter  $N$ , which was kept constant and is weak enough  
 590 to assume uniform ambient conditions, has a dominant effect on  $H_{nbl}$  due to its larger  
 591 scaling exponent in equation 2a. With realistic stratification,  $H_t$  remains less than 5%  
 592 of  $H_{nbl}$ , even for the experiment with the lowest  $B_0$  (experiment 14, where  $H_{nbl} = 21$   
 593 m from equation 2a). Thus, it is very likely that achieving a significant change in  $H_t$  would  
 594 require unrealistically high  $N$  values to reduce  $H_{nbl}$  to a scale comparable to the observed  
 595  $H_t$  for hydrothermal plumes.

## 596 4.2 Organization of the Flow Field

597 We focus on the relationships between the key flow variables in this transition re-  
 598 gion. Figure 8 presents the link between  $r$  and  $w$ , and  $b$  and  $w$  below ( $z = 0.29$  m) and  
 599 above ( $z = 5.0$  m) the transition height. Each experiment is related to its  $B_0$  value. Con-  
 600 sistent relationships indicate that the flow primarily depends on  $B_0$ . To limit spatial av-  
 601 eraging effects of cold fluid at the plume boundary, we restrict  $\sigma$  to  $10 \text{ cm s}^{-1}$ , which fil-  
 602 ters out experiments 12, 14, and 16 in Figure 8-b, d.

603 The organization is chaotic in the near-vent region, dominated by vent conditions  
 604 (Figure 8-a, c). In contrast, a clear organizational pattern emerges after reaching the pure  
 605 plume regime (Figure 8-b, d). The relationships between  $r$  and  $w$ , as well as  $b$  and  $w$ ,  
 606 both collapse to single power-law curves. Wang and Law (2002) showed that the mean  
 607 axial velocity and turbulent concentration fluctuations similarly collapse into Gaussian  
 608 curves for both forced and lazy plumes in pure plume regime.

609 In Figures 8-b and 8-d,  $B_0$  governs the overall organization of the flow, setting the  
 610 levels reached for each key variable above the transition region, where pure plume be-

611 havior is observed. The pattern does not depend on the excess force at the source. Con-  
 612 sequently, there are no scenarios where one quantity, such as  $w$ , becomes disproportion-  
 613 ately large while others, such as  $r$  or  $b$ , remain small. Instead, the system organizes it-  
 614 self to maintain consistency in the overall energy and momentum balance, with all vari-  
 615 ables adjusting together to reflect the level of  $B_0$  injected.

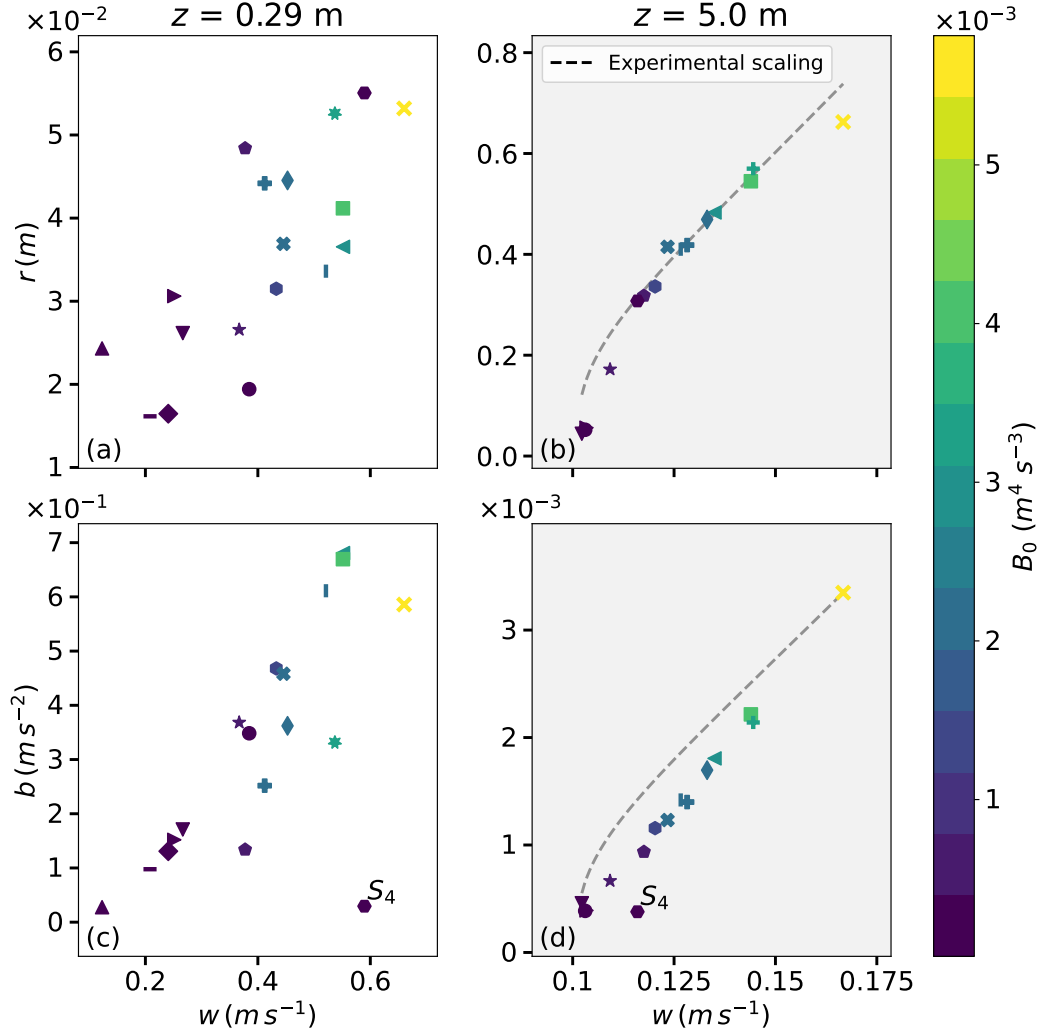


**Figure 8.** (a, b) Plume radius and (c, d) horizontal mean of buoyancy as a function of vertical velocity for  $\sigma = 10$  cm s<sup>-1</sup>. Each experiment is shown (a, c) below and (b, d) above the transition region identified in section 4.1. The symbols are colored according to the source buoyancy flux. Experimental scalings are plotted from (b) equation 8 and (d) equation 7b.

616 This is consistent with the buoyancy flux conservation approach in the MTT equa-  
 617 tions. The derivation of the theoretical model predicts an equilibrium level based solely  
 618 on  $B_0$  and the ambient stratification (equations 2). The scaling laws obtained from the  
 619 LES experiments reflect this behavior.

620 In a uniform environment, which is a valid assumption here (see section 3.1), the  
 621 right-hand term in equation 1-c vanishes, simplifying the MTT model to the analytical

622 solutions

$$r \propto z, \quad (6a)$$

$$b \propto B_0^{2/3} z^{-5/3}, \quad (6b)$$

$$w \propto B_0^{1/3} z^{-1/3}. \quad (6c)$$

623 These equations imply that the buoyancy flux is conserved at all heights. By combin-  
624 ing them, the relationships between the key plume variables are derived

$$r \propto B_0^{-1/3} z^{4/3} w, \quad (7a)$$

$$b \propto B_0^{1/3} z^{-4/3} w. \quad (7b)$$

625 A custom factor  $C_1(z) = 2.81 z^{-0.74}$  is applied to equation 7b to account for empiri-  
626 cal deviations observed in the flow field data, resulting in the scaling shown in Figure 8-  
627 d. It agrees within 20% with the factor predicted by Morton et al. (1956).

628 The agreement with the scaling laws improves with height as the distance from the  
629 transition region increases, indicating a breakdown of self-similarity in this region. Typ-  
630 ically, for plumes with  $\Gamma_0 \ll 0$ , such as solution S4 ( $\Gamma_0 = 0.01$  - experiment 15), equa-  
631 tion 7b incorrectly predicts high values of  $b$  for high values of  $w$ . Only when the highly  
632 forced plume dissipates its input momentum does it converge to the solution predicted  
633 by the scaling (Figure 8-c, d). However, even at  $z = 5$  m, the relationship between  $b$   
634 and  $w$  has not fully collapsed to the self-similarity solution. Taub et al. (2015) suggests  
635 that buoyancy fluctuations are influenced by source conditions over a longer range than  
636 velocity fluctuations.

637 Equation 6a shows the limitations of the analytical solution based on the assump-  
638 tion of a uniform environment. In this case, the plume radius is predicted to be inde-  
639 pendent of  $B_0$ , leading to an inconsistent relationship between  $r$ ,  $w$ , and  $B_0$  in equation 7a.  
640 In particular, increasing values of  $B_0$  result in decreasing plume radius for the analyt-  
641 ical solution, which is not consistent with the LES flow field. This discrepancy with the  
642 MTT model is due to its assumption of a constant spreading rate between plumes. The  
643 deviation observed in our results indicates a difference in the spreading rates, which is  
644 consistent with the experimental results of Kitamura and Sumita (2011). They observe  
645 that pure jets have a slightly higher spreading rate than plumes; however, this difference  
646 is generally considered to be small (Kotsovinos & List, 1977; Van Reeuwijk et al., 2016).

647 To align the scaling in equation 7a with the LES flow field, the dependence on  $B_0$   
648 is adjusted, and an empirical correction factor  $C_2(z)$  is introduced. This modified scal-  
649 ing is expressed as

$$r = C_2(z) B_0^{1/3} z^{4/3} w, \quad (8)$$

650 where  $C_2(z) = -0.27z + 3.9$ . This adjustment results in the scaling shown in Figure 8-  
651 b.

652 The overall agreement between the scaling and the LES experiments shows that,  
653 despite the strong influence of the near-vent region on the flow, the turbulent field can  
654 be simplified by scaling laws as plume quantities converge toward self-similarity. This  
655 indicates that in the far-field the MTT model captures the underlying physics based on  
656 the  $B_0$  value. The LES results highlight that  $B_0$  is the main controlling parameter, even  
657 in the exotic hydrothermal regime where high buoyancy flux is injected into weak strat-  
658 ification.

## 5 Discussion

### 5.1 Transition Region Observation

The transition region between vent conditions and the pure plume region is identified in an in-situ recording of a black smoker at the Tour Eiffel site. The video described below was captured by a ROV and is provided by the authors (Lemaréchal & Matabos, 2023). The comparison is summarized in Figure 9. The source observed here is the same as that used for the in-situ measurements in section 3.5, and experiment 9 is presented as the numerical counterpart.

We focus first on observations near the seafloor (between 15:10 and 15:44 in the video). The visible plume length is about 60 cm (Figure 9-b), while for this source,  $H_{\varepsilon_k} = 0.51$  m and  $H_{\alpha} = 1.53$  m. Compared to its numerical equivalent, this limits the analysis to region (1) in Figure 9-a, which is dominated by vent conditions. As the ROV ascends (between 16:15 and 18:54), the camera transitions from focusing on the near-vent region through the transition region (gray region labeled 2). At  $z \approx 2$  m, the camera reaches the fully buoyant region of the plume (gray region labeled 3 – around 17:30), where larger convective structures and fully three-dimensional turbulence dominate (according to LES data we get  $r \approx 0.4$  m,  $w \approx 5$  cm s<sup>-1</sup>). At this height, the mean temperature ( $T \approx 7$  °C) and the density gradient anomalies associated with the refractive index gradient decrease drastically. The light reflection from plume particles becomes insufficient to distinguish the plume clearly from its surroundings (e.g., at 17:50). In addition, the plume merges with those from neighboring sources, making numerical comparisons or in-situ studies of single source plumes extremely challenging.

Region (1) to (2) is the primary source of data for in-situ experiments, but this limitation introduces a bias in our understanding of the plume dynamics. By restricting observations to this specific region, we capture a view of the plume that is limited to its near-vent structure, which is strongly influenced by the transition from vent condition to pure plume behavior, where scaling laws fail.

### 5.2 Impact of Temperature Fluctuations on Tracer Proxies

Temperatures above 40°C have been documented as lethal to various organisms (Fisher, 1998; Bates et al., 2010; Lee et al., 2015). Given the high temperatures typical of black smokers, biotracer survival during transport through the plume might be expected to be unlikely. Consequently, studies often focus on stable environments that exclude such high-temperature conditions, e.g., Lee et al. (2015). However, LES results suggest that hydrothermal plumes could serve as a viable vector for biological material transport, as prolonged exposure to high temperatures is unlikely.

Below, we estimate how long particles transported within the first three meters of the rising plume are exposed to high and potentially lethal temperatures. To establish a high-temperature threshold of interest, we use the 40 °C criterion, which represents a reasonable estimate of the thermal tolerance limit for hydrothermal fauna. We distinguish between the plume’s inner core and its outer envelope, numerically defined as the closest cells to the plume boundary. The LES experiment is chosen to reflect the source conditions identified in section 3.5 (experiment 9 in Table 1). It provides an actual example of a source in close proximity to a dense faunal community (Van Audenhaege et al., 2022).

Due to computational limitations, an Eulerian approach was chosen over the ideal Lagrangian method. Fixed probes serve as proxies for the trajectory of a particle entrained in the plume. These probes are placed vertically at intervals corresponding to the mesh resolution, either along the plume axis or at its boundary. The envelope probes are positioned at the intersection of the horizontal plane with the contour of the plume vol-

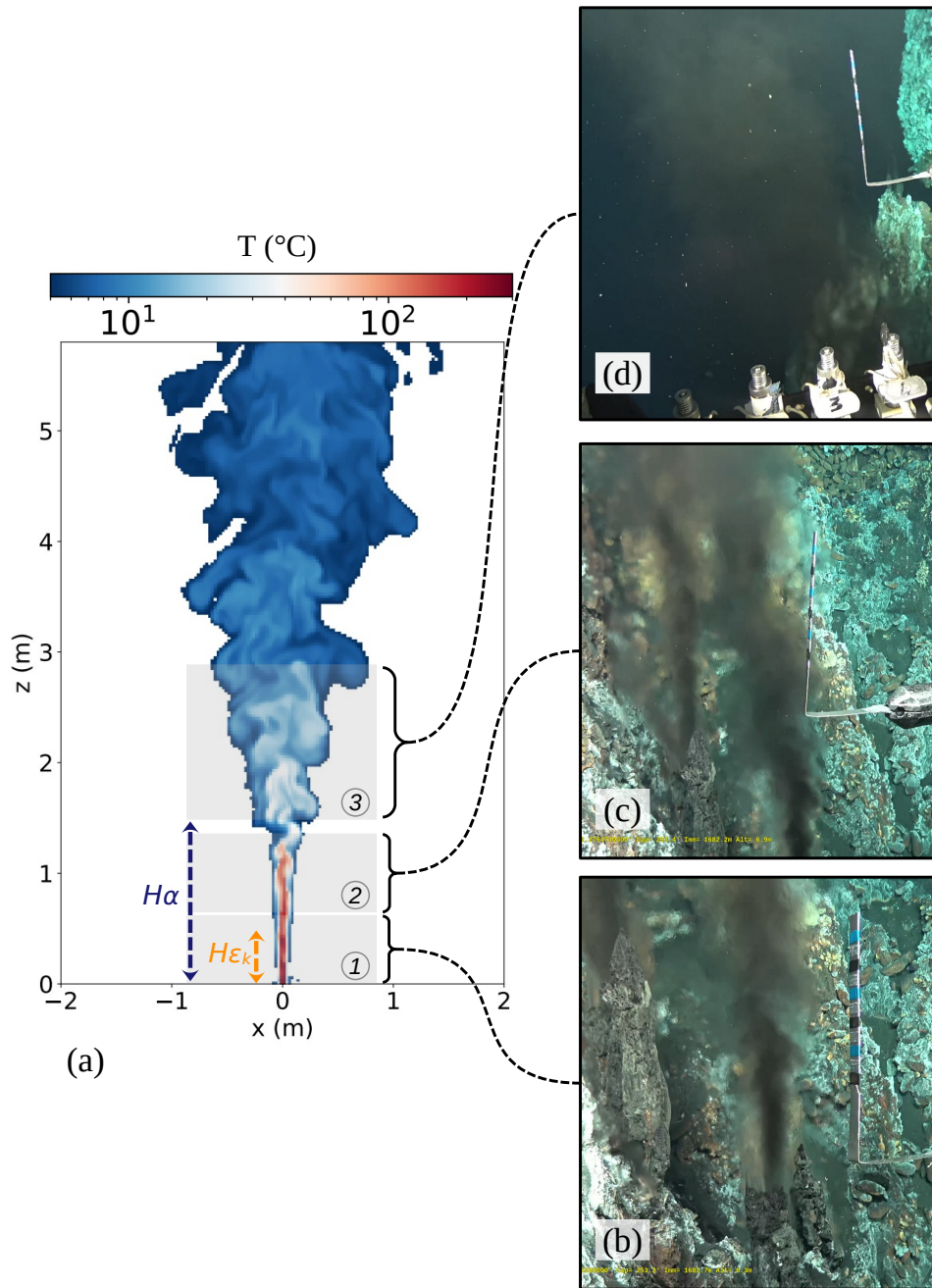


**Figure 9.** (a) Cross-sectional view of the instantaneous temperature field from a LES experiment (exp. 9), illustrating three types of regions corresponding to their respective in-situ observation windows as viewed during a video-recorded ROV exploration at Tour Eiffel. (b) The view corresponding to the height  $H_{\varepsilon_k}$ , (c) the view corresponding to  $H_\alpha$ , and (d) the region where the plume reached its fully convective turbulent state.

708 ume that satisfies the criterion  $\sigma = 0.1 \text{ m s}^{-1}$  on time average. This criterion is con-  
 709 sistent with that used to match the in-situ data, and selects a plume region with suffi-  
 710 cient vertical velocity to effectively advect materials. The bias introduced by sampling  
 711 the plume with a 1D line of probes is mitigated by the large number of measurements  
 712 taken over time: we use a sampling rate of 0.4 seconds over a duration of 14 minutes.

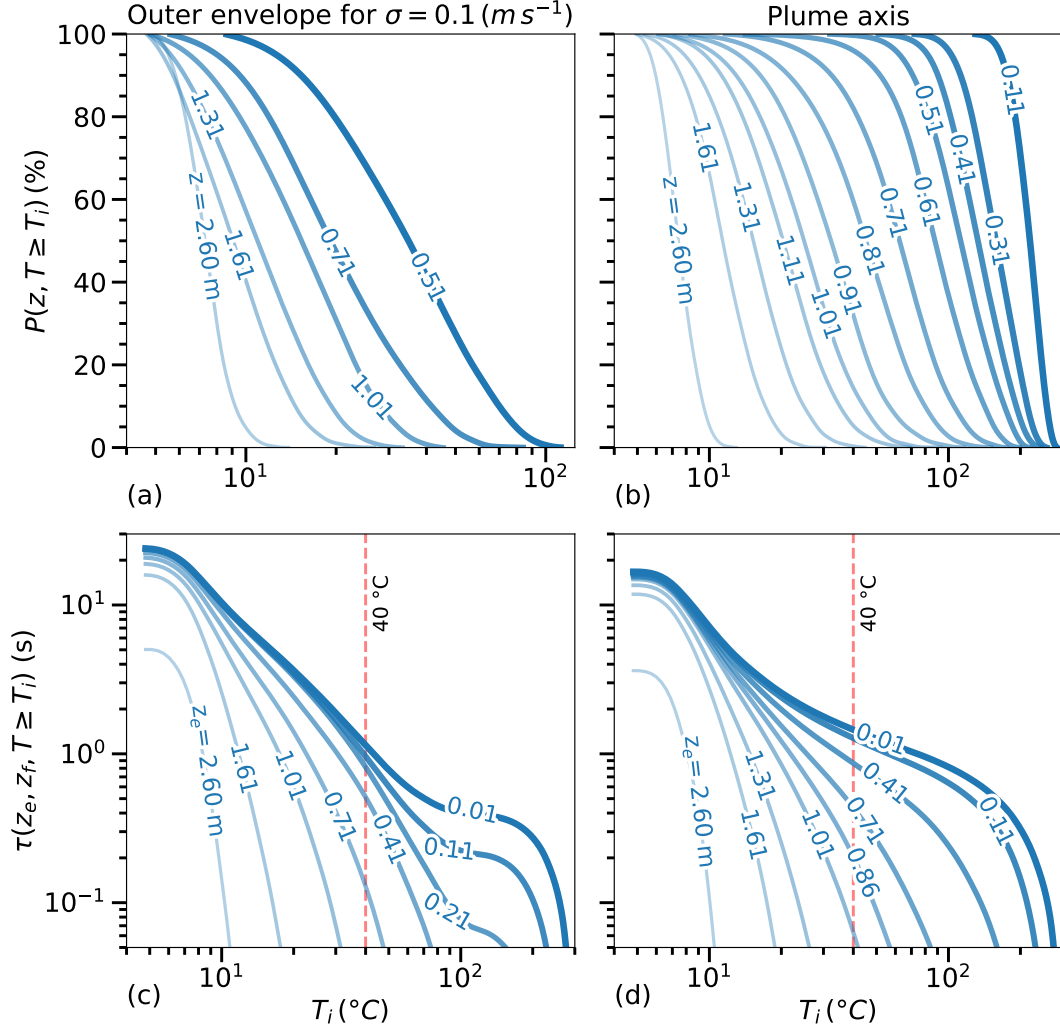


**Figure 10.** Complementary Cumulative Distribution Function (CCDF) of temperature at different heights  $z$  above the vent, for (a) the plume envelope selected by the criterion  $\sigma = 0.1 \text{ m s}^{-1}$  and (b) the plume axis. (c, d) The cumulative time  $\tau$  spent above each temperature  $T_i$  encountered in the hydrothermal fluid for trajectories along the vertical is shown in the same regions. Integration is performed for different starting entry heights  $z_e$  inside the plume up to  $z_f = 3 \text{ m}$ . (c, d) Plots are truncated below  $5 \times 10^{-2} \text{ s}$ .

713 Figure 10-a,b shows the CCDF,  $P(z, T \geq T_i)$ , derived from the time series of temper-  
 714 ature at each fixed probe location. At  $z = 80 \text{ cm}$ , the plume axis shows  $T > 40$   
 715 °C events representing 60 % of the time distribution, with a maximum temperature of  
 716 150 °C at this height (Figure 10-b). These high temperatures disappear from the core



717 after 1.30 m. Within the envelope, it takes 1 m to eliminate temperatures above 40 °C.  
718 At 70 cm, such temperatures occur 12 % of the time, peaking at 80 °C.

719 The probability distribution alone suggests that a tracer would encounter lethal  
720 temperatures in both the core and the envelope of the plume within the first meter above  
721 the vent. To investigate this further, we compute the cumulative time  $\tau$  (s). It is the time  
722 taken by a parcel entering the plume at height  $z_e$  to reach height  $z_f$ , following the tra-  
723 jectory traced by the 1D probe lines, with a temperature exceeding  $T_i$ . This computa-  
724 tion is performed in the envelope (Figure 10-c) and along the plume axis (Figure 10-d).  
725 The results are integrated from different starting entry heights  $z_e$  in the plume up to  $z_f =$   
726 3 m, where the temperature has decreased significantly, according to

$$\tau(z_e, z_f, T \geq T_i) = \int_{z_e}^{z_f} \frac{P(z, T \geq T_i)}{w_p(z)} dz, \quad (9)$$

727 where  $w_p(z)$  is the vertical speed at the probe location. The maximum  $\tau$  for each curve  
728 indicates the transit time between  $z_e$  and  $z_f$ .

729 The rationale for considering different starting heights  $z_e$  is that hydrothermal plumes  
730 are often associated with complex local topography, where the fluid comes into contact,  
731 providing different entry points for a tracer above the plume source. Below 30 cm, the  
732 envelope and core become indistinguishable, resulting in a characteristic bump in the en-  
733 velope curve, as the cumulative time reflects the core values (Figure 10-c), and  $w_p$  ex-  
734 ceeds the value chosen for  $\sigma$  in this region.

735 In the envelope, below  $z_e = 40$  cm, exposure to temperatures above 40 °C lasts  
736 for around 1 s, with significant exposure to higher temperatures, e.g., more than 0.3 s  
737 above 70 °C for  $z_e = 11$  cm. For a particle entering at 41 cm, exposure to temperatures  
738 above 40 °C lasts for 0.5 s, with only  $5 \times 10^{-2}$  s above 75 °C. Exposure to high temper-  
739 atures decreases significantly above 70 cm. A trajectory along the axis experiences 0.9  
740 s above 40 °C for  $z_e = 41$  cm, with a significant duration above very high temperatures  
741 compared to the envelope, e.g., 0.25 s above 100 °C. High temperature exposure along  
742 the plume axis becomes negligible only after 1 m. While particle paths are simplified for  
743 practical purposes by considering 1D lines, it is important to note that particles could  
744 be advected through both regions discussed, and it is essential to assess the viability of  
745 tracers as a percentage of success. Nevertheless, both the core and the envelope of the  
746 plume show minimal exposure to high temperatures for a particle entrained 1 m above  
747 the vent. The envelope is a more favorable region for sustained transport for an entry  
748 closer to the vent ( $z_e = 40$  cm), considering the temperature levels and time exposure  
749 ratio, compared to the plume centerline.

750 These results support the findings of Kim et al. (1994), who demonstrated through  
751 dye experiments and the MTT model that a single black smoker can enable substantial  
752 vertical transport of larvae, opening pathways to habitats typically inaccessible to near-  
753 bottom larvae.

## 754 6 Conclusions

755 Hydrothermal plumes inject a high buoyancy flux into weak stratification, rising  
756 from centimeter-scale vents to heights of several hundred meters (Lavelle et al., 2013).  
757 They play a key role in vent fields but have been poorly characterized in the near-vent  
758 region. To study these plumes, we used a LES approach with adaptive mesh refinement  
759 to achieve centimeter-scale resolution within a 6 m domain above the vent. Several key  
760 points can be highlighted.

761 First, a typical black smoker (forced plume) is studied to quantify the mean flow  
762 and spatial fluctuations, which are difficult to measure in deep-sea vent fields. The mean  
763 temperature decreases sharply from  $T_0 = 300$  °C to  $T - T_a = 1.5$  °C at  $z = 5$  m, and

764 the velocity decreases from  $w_0 = 70 \text{ cm s}^{-1}$  to  $w = 7 \text{ cm s}^{-1}$ . This results in a sub-  
 765 substantial volume flow of  $Q = 0.25 \text{ m}^3 \text{ s}^{-1}$  at  $z = 5 \text{ m}$ . The plume expands at a nearly  
 766 constant spreading rate. The results compare well with in-situ measurements. While lazy  
 767 plumes initially accelerate (Marjanovic et al., 2017), we show that forced plumes in the  
 768 hydrothermal regime also accelerate due to significant buoyancy, reaching  $w = 1.14 \text{ m}$   
 769  $\text{s}^{-1}$ . Numerical approaches to hydrothermal plumes often model a diluted point source  
 770 above the vent, e.g., Adams and Di Iorio (2021); however, approximating a uniform source  
 771 below  $z = 5 \text{ m}$  fails to capture the flow dynamics, especially since turbulence is fully  
 772 developed at this height.

773 Secondly, we show that the entrainment rate exhibits strong vertical and tempo-  
 774 ral variability, associated with the intense mixing required to dissipate the high source  
 775 buoyancy flux. The overall value in the near-field is  $\alpha = 0.19$ , which is significantly higher  
 776 than the classical value of  $\alpha = 0.12$  for a pure plume (Van Reeuwijk & Craske, 2015;  
 777 Richardson & Hunt, 2022). However, the values vary significantly in the vertical, from  
 778  $\alpha = 0.07$  in the jet-like plume region to  $\alpha = 0.15$  in the pure plume region, with much  
 779 larger values in between. The large variations in  $\alpha(z, t)$  are linked to the coherent struc-  
 780 tures of the turbulent field. Variations reaching up to 90% above the mean profile di-  
 781 lute and homogenize the temperature anomaly distribution, contributing to the flow de-  
 782 celeration. It highlights the main limitation of the MTT model (Morton et al., 1956):  
 783  $\alpha$  cannot be assumed constant in the near-field. A more appropriate approach would in-  
 784 corporate the work of Wang and Law (2002), who developed a second-order integral model  
 785 to account for entrainment rate variations, where  $\alpha(z)$  is treated as a function of the lo-  
 786 cal Richardson number.

787 Extreme temperatures ( $T > 100 \text{ }^\circ\text{C}$ ) occur for  $z < 2 \text{ m}$ , coinciding with the abil-  
 788 ity of the plume to entrain biotracers from the seafloor. While the limited biological tol-  
 789 erance to high temperatures suggests that particle survival during transport through the  
 790 plume is unlikely, our study offers a different perspective. For a proxy tracer, exposure  
 791 times at  $T > 40 \text{ }^\circ\text{C}$  can be as short as  $0.5 \text{ s}$  in the plume envelope, depending on the  
 792 height of entrainment, decreasing to  $5 \times 10^{-2} \text{ s}$  above  $T = 75 \text{ }^\circ\text{C}$ . This challenges the  
 793 concept of lethal temperatures in dynamic flows. Hydrothermal plumes could thus act  
 794 as viable vectors for the transport of biological material from the seafloor, supporting  
 795 the findings of Kim et al. (1994), provided more is known about the ability of the fauna  
 796 to withstand such conditions for very short periods.

797 Finally, the sensitivity to source parameters is investigated for the forced and lazy  
 798 plume regimes. We show that the adjustment from the near-vent region, dominated by  
 799 source conditions, to the far-field, pure plume regime, leads to the breakdown of self-similar  
 800 plume behavior in this transition region. This prevents the application of the theoret-  
 801 ical model of Morton et al. (1956) in the transition region, which extends from  $z = 0.25$   
 802  $\text{m}$  to  $z = 2.15 \text{ m}$ . The transition height shows little sensitivity to the plume regime and  
 803 would require unrealistic changes in stratification to be significantly affected. Plumes ob-  
 804 served at the scale of hydrothermal edifices are typically in a transition state, which may  
 805 introduce bias into experimental studies at this depth. In the far-field, plumes converge  
 806 to self-similarity and can be described by scalings 7b and 8 derived from plume theory.  
 807 While the mean quantities do not agree well with the MTT model predictions, the flow  
 808 field in the pure plume region agrees with the MTT model approach and is primarily or-  
 809 ganized according to the source buoyancy flux.

## 810 Data Availability Statement

811 The real-time sequence of the turbulent field observed with the  $\lambda_2$  technique is avail-  
 812 able on Zenodo at <https://doi.org/10.5281/zenodo.13829868> (Lemaréchal et al., 2024a).  
 813 The in-situ recording of a black smoker can be accessed online in 720p resolution at [https://](https://video.ifremer.fr/video?id=52548)  
 814 [video.ifremer.fr/video?id=52548](https://video.ifremer.fr/video?id=52548) and downloaded in 4K resolution on SEANOE at

815 <https://doi.org/10.17882/103869> (Lemaréchal & Matabos, 2023). A code to com-  
 816 pute the parametric EOS is available on Zenodo at [https://doi.org/10.5281/zenodo](https://doi.org/10.5281/zenodo.14332032)  
 817 .14332032 (Lemaréchal et al., 2024b).

### 818 Acknowledgments

819 The authors acknowledge support from Université de Bretagne Occidentale, the iAtlantic  
 820 project (Grant #818123) supported by the European Union’s Horizon 2020 (H2020) pro-  
 821 gram, the LOPS, and the Interdisciplinary Graduate School for the Blue Planet project  
 822 (ANR-17-EURE-0015). This work was performed using HPC resources from GENCI-  
 823 TGCC (Grant #2022-A0090112051). We warmly thank the crews of *L’Atalante* who par-  
 824 ticipated in the MoMARSAT cruises. We also acknowledge M. Matabos, P.-M. Sarradin,  
 825 and M. Cannat for co-leading and managing the MoMARSAT cruises and the EMSO-  
 826 Azores observatory.

### 827 Appendix A Parametric EOS

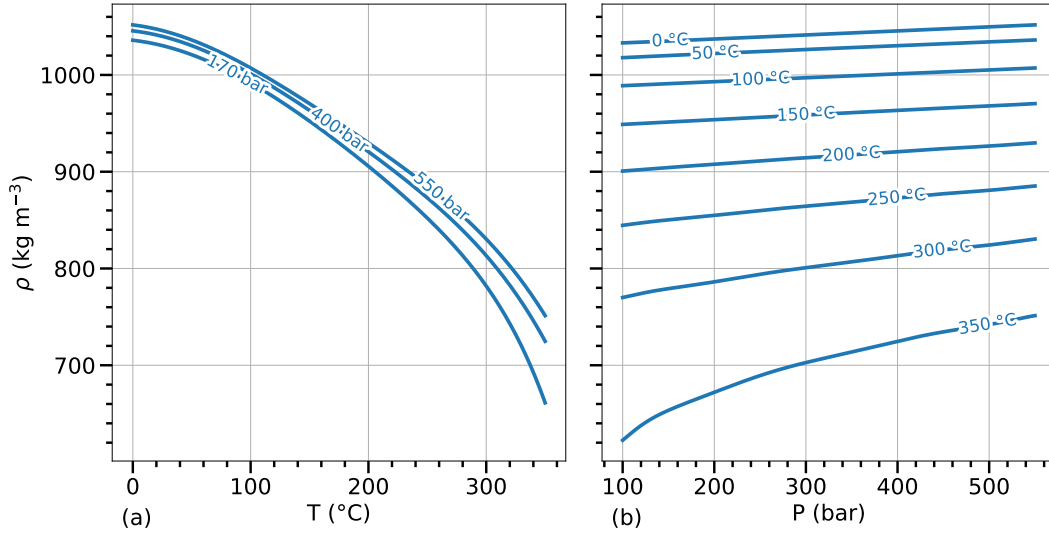


**Figure A1.** (a) Density of seawater vs. temperature calculated by equation A1 for different levels of pressure. (b) Density vs pressure for different levels of temperature.

828 This section presents the Equation Of State (EOS) developed for hydrothermal flu-  
 829 ids. The EOS is valid in the range of 100–550 bar and 0–350 °C at  $S_A = 35.2 \text{ g kg}^{-1}$ .  
 830 A plot of density for different pressure and temperature ranges is shown in Figure A1.

831 The density  $\rho$  (kg m<sup>-3</sup>) as a function of absolute temperature  $T$  (°C) and abso-  
 832 lute pressure  $P$  (bar) is given by

$$\rho(T, P) = A(P) \exp(-B(P)T) + C(P) + D(P) \exp\left(-\frac{(T - E(P))^2}{2F(P)^2}\right), \quad (\text{A1})$$

833 where  $A(P) \dots F(P)$  are polynomials in  $P$  of the form

$$X(P) = \sum_{i=0}^8 c_i P^{8-i}, \quad (\text{A2})$$

834 with  $c_i$  being the polynomial coefficients given in Table A1 for each parameter. A code  
 835 sample to compute this equation is provided by the authors (Lemaréchal et al., 2024b).  
 836 To spare computing resources during calculations, we recommend generating an EOS ta-  
 837 ble with a fixed step for efficient data interpolation through array indexing.

**Table A1.** Polynomial coefficients of equation A2

	0	1	2	3	4	5	6	7	8
A	-7.01307390e-21	1.95660070e-17	-2.23352820e-14	1.30848310e-11	-3.97395990e-09	5.53535930e-07	-3.96405330e-05	1.37810860e-03	-1.62833820e-02
B	-2.04801770e-22	5.85654850e-19	-7.17814260e-16	4.93110400e-13	-2.08500570e-10	5.61590670e-08	-9.67436850e-06	1.04954760e+03	-7.55052580e-02
C	-9.08091870e-18	2.56711040e-14	-3.09991740e-11	2.08730680e-08	-8.57874330e-06	2.21278690e-03	-3.54404280e-01	3.36599270e+01	-7.59305030e+02
D	9.14772610e-18	-2.58613080e-14	3.12300980e-11	-2.10288630e-08	8.64259430e-06	-2.22918380e-03	3.57047310e-01	-3.38666710e+01	1.79999190e+03
E	-2.57551460e-19	7.36404340e-16	-9.02945380e-13	6.20751900e-10	-2.62358970e-07	7.01422040e-05	-1.17048000e-02	1.14665420e+00	-7.20442180e+01
F	2.80580730e-18	-7.95146740e-15	9.63263680e-12	-6.51411210e-09	2.69367930e-06	-7.01266430e-04	1.14048660e-01	-1.11301910e+01	7.25953200e+02

## 838 References

- 839 Adams, I., & Di Iorio, D. (2021). Turbulence properties of a deep-sea hydrothermal  
 840 plume in a time-variable cross-flow: Field and model comparisons for dante in  
 841 the main endeavour field. *Journal of Geophysical Research: Oceans*, *126*(9),  
 842 e2020JC016638. doi: <https://doi.org/10.1029/2020JC016638>
- 843 Barreyre, T., Escartín, J., Garcia, R., Cannat, M., Mittelstaedt, E., & Prados, R.  
 844 (2012). Structure, temporal evolution, and heat flux estimates from the lucky  
 845 strike deep-sea hydrothermal field derived from seafloor image mosaics. *Geo-*  
 846 *chemistry, Geophysics, Geosystems*, *13*(4). doi: [https://doi.org/10.1029/](https://doi.org/10.1029/2011GC003990)  
 847 [2011GC003990](https://doi.org/10.1029/2011GC003990)
- 848 Barreyre, T., Escartín, J., Sohn, R. A., Cannat, M., Ballu, V., & Crawford, W. C.  
 849 (2014). Temporal variability and tidal modulation of hydrothermal exit-  
 850 fluid temperatures at the lucky strike deep-sea vent field, mid-atlantic ridge.  
 851 *Journal of Geophysical Research: Solid Earth*, *119*(4), 2543–2566. doi:  
 852 <https://doi.org/10.1002/2013JB010478>
- 853 Bates, A. E., Lee, R. W., Tunnicliffe, V., & Lamare, M. D. (2010). Deep-sea hy-  
 854 drothermal vent animals seek cool fluids in a highly variable thermal envi-  
 855 ronment. *Nature Communications*, *1*(1), 14. doi: [https://doi.org/10.1038/](https://doi.org/10.1038/ncomms1014)  
 856 [ncomms1014](https://doi.org/10.1038/ncomms1014)
- 857 Bell, J. B., Colella, P., & Glaz, H. M. (1989). A second-order projection method for  
 858 the incompressible navier-stokes equations. *Journal of computational physics*,  
 859 *85*(2), 257–283. doi: [https://doi.org/10.1016/0021-9991\(89\)90151-4](https://doi.org/10.1016/0021-9991(89)90151-4)
- 860 Bemis, K. G., Silver, D., Xu, G., Light, R., Jackson, D., Jones, C., ... Liu, L.  
 861 (2015). The path to covis: A review of acoustic imaging of hydrothermal  
 862 flow regimes. *Deep Sea Research Part II: Topical Studies in Oceanography*,  
 863 *121*, 159–176. doi: <https://doi.org/10.1016/j.dsr2.2015.06.002>
- 864 Bischoff, J. L., & Rosenbauer, R. J. (1985). An empirical equation of state for hy-  
 865 drothermal seawater (3.2 percent nacl). *American Journal of Science*, *285*(8),  
 866 725–763. doi: <https://doi.org/10.2475/ajs.285.8.725>
- 867 Chavagnac, V., Ali, H. S., Jeandel, C., Leleu, T., Destrigneville, C., Castillo,  
 868 A., ... others (2018). Sulfate minerals control dissolved rare earth ele-  
 869 ment flux and nd isotope signature of buoyant hydrothermal plume (emso-  
 870 azores, 37 n mid-atlantic ridge). *Chemical Geology*, *499*, 111–125. doi:  
 871 <https://doi.org/10.1016/j.chemgeo.2018.09.021>
- 872 Ciriello, F., & Hunt, G. (2020). Analytical solutions and virtual origin cor-  
 873 rections for forced, pure and lazy turbulent plumes based on a univer-  
 874 sal entrainment function. *Journal of Fluid Mechanics*, *893*, A12. doi:  
 875 <https://doi.org/10.1017/jfm.2020.225>

- 876 Cotte, L., Chavagnac, V., Pelleter, E., Laës-Huon, A., Cathalot, C., Dulaquais, G.,  
877 ... Waeles, M. (2020). Metal partitioning after in situ filtration at deep-sea  
878 vents of the lucky strike hydrothermal field (emso-azores, mid-atlantic ridge, 37  
879 n). *Deep Sea Research Part I: Oceanographic Research Papers*, 157, 103204.
- 880 Crone, T. J., McDuff, R. E., & Wilcock, W. S. (2008). Optical plume velocimetry: A  
881 new flow measurement technique for use in seafloor hydrothermal systems. *Ex-*  
882 *periments in fluids*, 45, 899–915. doi: <https://doi.org/10.1007/s00348-008-0508>  
883 -2
- 884 Davies, J. H., & Davies, D. R. (2010). Earth’s surface heat flux. *Solid earth*, 1(1),  
885 5–24. doi: <https://doi.org/10.5194/se-1-5-2010>
- 886 Devenish, B., Rooney, G., & Thomson, D. (2010). Large-eddy simulation of a buoy-  
887 ant plume in uniform and stably stratified environments. *Journal of Fluid Me-*  
888 *chanics*, 652, 75–103. doi: <https://doi.org/10.1017/S0022112010000017>
- 889 Fiedler, H. (1988). Coherent structures in turbulent flows. *Progress in Aerospace*  
890 *Sciences*, 25(3), 231–269. doi: [https://doi.org/10.1016/0376-0421\(88\)90001-2](https://doi.org/10.1016/0376-0421(88)90001-2)
- 891 Fisher, C. R. (1998). Temperature and sulphide tolerance of hydrothermal vent  
892 fauna. *Cah. Biol. Mar*, 39(3-4), 283–286.
- 893 Fontaine, F. J., Cannat, M., Escartin, J., & Crawford, W. C. (2014). Along-axis  
894 hydrothermal flow at the axis of slow spreading mid-ocean ridges: Insights  
895 from numerical models of the lucky strike vent field (mar). *Geochemistry,*  
896 *Geophysics, Geosystems*, 15(7), 2918–2931. doi: [https://doi.org/10.1002/](https://doi.org/10.1002/2014GC005372)  
897 [2014GC005372](https://doi.org/10.1002/2014GC005372)
- 898 Fox, D. G. (1970). Forced plume in a stratified fluid. *Journal of Geophysical Re-*  
899 *search*, 75(33), 6818–6835. doi: <https://doi.org/10.1029/JC075i033p06818>
- 900 Gao, X., Dong, C., Liang, J., Yang, J., Li, G., Wang, D., & McWilliams, J. C.  
901 (2019). Convective instability-induced mixing and its parameteriza-  
902 tion using large eddy simulation. *Ocean Modelling*, 137, 40–51. doi:  
903 <https://doi.org/10.1016/j.ocemod.2019.03.008>
- 904 Girard, F., Sarrazin, J., Arnaubec, A., Cannat, M., Sarradin, P.-M., Wheeler, B., &  
905 Matabos, M. (2020). Currents and topography drive assemblage distribution  
906 on an active hydrothermal edifice. *Progress in oceanography*, 187, 102397. doi:  
907 <https://doi.org/10.1016/j.pocean.2020.102397>
- 908 Hargreaves, D. M., Scase, M. M., & Evans, I. (2012). A simplified computational  
909 analysis of turbulent plumes and jets. *Environmental fluid mechanics*, 12, 555–  
910 578. doi: <https://doi.org/10.1007/s10652-012-9250-7>
- 911 Hunt, G., & Kaye, N. (2001). Virtual origin correction for lazy turbulent plumes.  
912 *Journal of Fluid Mechanics*, 435, 377–396. doi: [https://doi.org/10.1017/](https://doi.org/10.1017/S0022112001003871)  
913 [S0022112001003871](https://doi.org/10.1017/S0022112001003871)
- 914 Hunt, G., & Kaye, N. (2005). Lazy plumes. *Journal of Fluid Mechanics*, 533, 329–  
915 338. doi: <https://doi.org/10.1017/S002211200500457X>
- 916 IOC, SCOR, IAPSO, et al. (2010). The international thermodynamic equation of  
917 seawater, 2010: calculation and use of thermodynamic properties.
- 918 Jeong, J., & Hussain, F. (1995). On the identification of a vortex. *Journal of fluid*  
919 *mechanics*, 285, 69–94. doi: <https://doi.org/10.1017/S0022112095000462>
- 920 Jiang, H., & Breier, J. A. (2014). Physical controls on mixing and transport  
921 within rising submarine hydrothermal plumes: A numerical simulation study.  
922 *Deep Sea Research Part I: Oceanographic Research Papers*, 92, 41–55. doi:  
923 <https://doi.org/10.1016/j.dsr.2014.06.006>
- 924 Kaye, N. (2008). Turbulent plumes in stratified environments: A review of recent  
925 work. *Atmosphere-ocean*, 46(4), 433–441. doi: <https://doi.org/10.3137/ao>  
926 [.460404](https://doi.org/10.3137/ao)
- 927 Kim, S. L., Mullineaux, L. S., & Helfrich, K. R. (1994). Larval dispersal via en-  
928 trainment into hydrothermal vent plumes. *Journal of Geophysical Research:*  
929 *Oceans*, 99(C6), 12655–12665. doi: <https://doi.org/10.1029/94JC00644>
- 930 Kitamura, S., & Sumita, I. (2011). Experiments on a turbulent plume: Shape anal-

- yses. *Journal of Geophysical Research: Solid Earth*, 116(B3). doi: <https://doi.org/10.1029/2010JB007633>
- Koschinsky, A., Garbe-Schönberg, D., Sander, S., Schmidt, K., Gennerich, H.-H., & Strauss, H. (2008). Hydrothermal venting at pressure-temperature conditions above the critical point of seawater, 5 s on the mid-atlantic ridge. *Geology*, 36(8), 615–618. doi: <https://doi.org/10.1130/G24726A.1>
- Kotsovinos, N. E., & List, E. J. (1977). Plane turbulent buoyant jets. part 1. integral properties. *Journal of Fluid Mechanics*, 81(1), 25–44. doi: <https://doi.org/10.1017/S002211207700189X>
- Lavelle, J., Di Iorio, D., & Rona, P. (2013). A turbulent convection model with an observational context for a deep-sea hydrothermal plume in a time-variable cross flow. *Journal of Geophysical Research: Oceans*, 118(11), 6145–6160. doi: <https://doi.org/10.1002/2013JC009165>
- Lee, R. W., Robert, K., Matabos, M., Bates, A. E., & Juniper, S. K. (2015). Temporal and spatial variation in temperature experienced by macrofauna at main endeavour hydrothermal vent field. *Deep Sea Research Part I: Oceanographic Research Papers*, 106, 154–166. doi: <https://doi.org/10.1016/j.dsr.2015.10.004>
- Lemaréchal, C., & Matabos, M. (2023). *Recording of a black smoker at the tour eiffel vent field during momarsat2023*. SEANO. doi: <https://doi.org/10.17882/103869>
- Lemaréchal, C., Rouillet, G., & Gula, J. (2024a). *Coherent structures of a hydrothermal buoyant plume in the near-field obtained through les at ultra-high resolution*. Zenodo. doi: <https://doi.org/10.5281/zenodo.13829868>
- Lemaréchal, C., Rouillet, G., & Gula, J. (2024b). *Parametric equation of state of seawater for hydrothermal vent conditions*. Zenodo. doi: <https://doi.org/10.5281/zenodo.14332032>
- Marjanovic, G., Taub, G., & Balachandar, S. (2017). On the evolution of the plume function and entrainment in the near-source region of lazy plumes. *Journal of Fluid Mechanics*, 830, 736–759. doi: <https://doi.org/10.1017/jfm.2017.622>
- Matulka, A., López, P., Redondo, J., & Tarquis, A. (2014). On the entrainment coefficient in a forced plume: quantitative effects of source parameters. *Nonlinear processes in geophysics*, 21(1), 269–278. doi: <https://doi.org/10.5194/npg-21-269-2014>
- McDougall, T. J., Jackett, D. R., Wright, D. G., & Feistel, R. (2003). Accurate and computationally efficient algorithms for potential temperature and density of seawater. *Journal of Atmospheric and Oceanic Technology*, 20(5), 730–741. doi: [https://doi.org/10.1175/1520-0426\(2003\)20%3C730:AAACEAF%3E2.0.CO;2](https://doi.org/10.1175/1520-0426(2003)20%3C730:AAACEAF%3E2.0.CO;2)
- Mittelstaedt, E., Escartín, J., Gracias, N., Olive, J.-A., Barreyre, T., Davaille, A., ... Garcia, R. (2012). Quantifying diffuse and discrete venting at the tour eiffel vent site, lucky strike hydrothermal field. *Geochemistry, Geophysics, Geosystems*, 13(4). doi: <https://doi.org/10.1029/2011GC003991>
- Morton, B. (1959). Forced plumes. *Journal of Fluid mechanics*, 5(1), 151–163. doi: <https://doi.org/10.1017/S002211205900012X>
- Morton, B., & Middleton, J. (1973). Scale diagrams for forced plumes. *Journal of Fluid Mechanics*, 58(1), 165–176. doi: <https://doi.org/10.1017/S002211207300220X>
- Morton, B., Taylor, G. I., & Turner, J. S. (1956). Turbulent gravitational convection from maintained and instantaneous sources. *Proceedings of the Royal Society of London. Series A. Mathematical and Physical Sciences*, 234(1196), 1–23. doi: <https://doi.org/10.1098/rspa.1956.0011>
- Mullineaux, L. S., & France, S. C. (1995). Dispersal mechanisms of deep-sea hydrothermal vent fauna. *Geophysical Monograph Series*, 91, 408–424. doi: <https://doi.org/10.1029/GM091p0408>

- 986 Pham, M., Plourde, F. d. r., & Kim, S. D. (2005). Three-dimensional characteriza-  
 987 tion of a pure thermal plume. *J. Heat Transfer*, *127*(6), 624–636. doi: <https://doi.org/10.1115/1.1863275>  
 988
- 989 Plourde, F., Pham, M. V., Kim, S. D., & Balachandar, S. (2008). Direct nu-  
 990 merical simulations of a rapidly expanding thermal plume: structure and  
 991 entrainment interaction. *Journal of Fluid Mechanics*, *604*, 99–123. doi:  
 992 <https://doi.org/10.1017/S0022112008001006>
- 993 Popinet, S. (2003). Gerris: a tree-based adaptive solver for the incompressible eu-  
 994 ler equations in complex geometries. *Journal of computational physics*, *190*(2),  
 995 572–600. doi: [https://doi.org/10.1016/S0021-9991\(03\)00298-5](https://doi.org/10.1016/S0021-9991(03)00298-5)
- 996 Popinet, S. (2009). An accurate adaptive solver for surface-tension-driven interfacial  
 997 flows. *Journal of Computational Physics*, *228*(16), 5838–5866. doi: <https://doi.org/10.1016/j.jcp.2009.04.042>  
 998
- 999 Popinet, S. (2013). *The basilisk code*. Retrieved from <http://basilisk.fr/>
- 1000 Popinet, S. (2015). A quadtree-adaptive multigrid solver for the serre–green–naghdī  
 1001 equations. *Journal of Computational Physics*, *302*, 336–358. doi: <https://doi.org/10.1016/j.jcp.2015.09.009>  
 1002
- 1003 Priestley, C., & Ball, F. (1955). Continuous convection from an isolated source of  
 1004 heat. *Quarterly Journal of the Royal Meteorological Society*, *81*(348), 144–157.  
 1005 doi: <https://doi.org/10.1002/qj.49708134803>
- 1006 Richardson, J., & Hunt, G. R. (2022). What is the entrainment coefficient of a pure  
 1007 turbulent line plume? *Journal of Fluid Mechanics*, *934*, A11. doi: <https://doi.org/10.1017/jfm.2021.1070>  
 1008
- 1009 Safarov, J., Millero, F., Feistel, R., Heintz, A., & Hassel, E. (2009). Thermody-  
 1010 namic properties of standard seawater: extensions to high temperatures and  
 1011 pressures. *Ocean Science*, *5*(3), 235–246. doi: <https://doi.org/10.5194/os-5-235-2009>  
 1012
- 1013 Sarrazin, J., Rodier, P., Tivey, M. K., Singh, H., Schultz, A., & Sarradin, P.-M.  
 1014 (2009). A dual sensor device to estimate fluid flow velocity at diffuse hy-  
 1015 drothermal vents. *Deep Sea Research Part I: Oceanographic Research Papers*,  
 1016 *56*(11), 2065–2074. doi: <https://doi.org/10.1016/j.dsr.2009.06.008>
- 1017 Sclater, J., Jaupart, C., & Galson, D. (1980). The heat flow through oceanic and  
 1018 continental crust and the heat loss of the earth. *Reviews of Geophysics*, *18*(1),  
 1019 269–311. doi: <https://doi.org/10.1029/RG018i001p00269>
- 1020 Shabbir, A., & George, W. K. (1994). Experiments on a round turbulent buoyant  
 1021 plume. *Journal of Fluid Mechanics*, *275*, 1–32. doi: <https://doi.org/10.1017/S0022112094002260>  
 1022
- 1023 Sun, H., Feistel, R., Koch, M., & Markoe, A. (2008). New equations for density, en-  
 1024 tropy, heat capacity, and potential temperature of a saline thermal fluid. *Deep*  
 1025 *Sea Research Part I: Oceanographic Research Papers*, *55*(10), 1304–1310. doi:  
 1026 <https://doi.org/10.1016/j.dsr.2008.05.011>
- 1027 Tao, Y., Rosswog, S., & Brüggem, M. (2013). A simulation modeling approach to hy-  
 1028 drothermal plumes and its comparison to analytical models. *Ocean Modelling*,  
 1029 *61*, 68–80. doi: <https://doi.org/10.1016/j.ocemod.2012.10.001>
- 1030 Taub, G., Lee, H., Balachandar, S., & Sherif, S. (2015). An examination of the  
 1031 high-order statistics of developing jets, lazy and forced plumes at various axial  
 1032 distances from their source. *Journal of Turbulence*, *16*(10), 950–978. doi:  
 1033 <https://doi.org/10.1080/14685248.2015.1008006>
- 1034 Van Audenhaege, L., Matabos, M., Brind’Amour, A., Drugmand, J., Laës-Huon,  
 1035 A., Sarradin, P.-M., & Sarrazin, J. (2022). Long-term monitoring reveals  
 1036 unprecedented stability of a vent mussel assemblage on the mid-atlantic  
 1037 ridge. *Progress in Oceanography*, *204*, 102791. doi: <https://doi.org/10.1016/j.pocean.2022.102791>  
 1038
- 1039 Van Dover, C. L. (2002). Community structure of mussel beds at deep-sea hy-  
 1040 drothermal vents. *Marine Ecology Progress Series*, *230*, 137–158. doi:

- 1041 doi:10.3354/meps230137  
1042 Van Reeuwijk, M., & Craske, J. (2015). Energy-consistent entrainment relations for  
1043 jets and plumes. *Journal of Fluid Mechanics*, *782*, 333–355. doi: [https://doi](https://doi.org/10.1017/jfm.2015.534)  
1044 [.org/10.1017/jfm.2015.534](https://doi.org/10.1017/jfm.2015.534)  
1045 Van Reeuwijk, M., Salizzoni, P., Hunt, G. R., & Craske, J. (2016). Turbulent trans-  
1046 port and entrainment in jets and plumes: a dns study. *Physical Review Fluids*,  
1047 *1*(7), 074301. doi: <https://doi.org/10.1103/PhysRevFluids.1.074301>  
1048 Vic, C., Gula, J., Roulet, G., & Pradillon, F. (2018). Dispersion of deep-sea hy-  
1049 drothermal vent effluents and larvae by submesoscale and tidal currents. *Deep*  
1050 *Sea Research Part I: Oceanographic Research Papers*, *133*, 1–18. doi: [https://](https://doi.org/10.1016/j.dsr.2018.01.001)  
1051 [doi.org/10.1016/j.dsr.2018.01.001](https://doi.org/10.1016/j.dsr.2018.01.001)  
1052 Vreman, A. (2004). An eddy-viscosity subgrid-scale model for turbulent shear flow:  
1053 Algebraic theory and applications. *Physics of fluids*, *16*(10), 3670–3681. doi:  
1054 <https://doi.org/10.1063/1.1785131>  
1055 Wang, H., & Law, A. W.-k. (2002). Second-order integral model for a round turbu-  
1056 lent buoyant jet. *Journal of Fluid Mechanics*, *459*, 397–428. doi: [https://doi](https://doi.org/10.1017/S0022112002008157)  
1057 [.org/10.1017/S0022112002008157](https://doi.org/10.1017/S0022112002008157)  
1058 Winters, K. B., Lombard, P. N., Riley, J. J., & D’Asaro, E. A. (1995). Available po-  
1059 tential energy and mixing in density-stratified fluids. *Journal of Fluid Mechan-*  
1060 *ics*, *289*, 115–128. doi: <https://doi.org/10.1017/S002211209500125X>  
1061 Woods, A. W. (2010). Turbulent plumes in nature. *Annual Review of Fluid*  
1062 *Mechanics*, *42*(1), 391–412. doi: [https://doi.org/10.1146/annurev-fluid-121108](https://doi.org/10.1146/annurev-fluid-121108-145430)  
1063 [-145430](https://doi.org/10.1146/annurev-fluid-121108-145430)  
1064 Wykes, M. S. D., Hughes, G. O., & Dalziel, S. B. (2015). On the meaning of mix-  
1065 ing efficiency for buoyancy-driven mixing in stratified turbulent flows. *Journal*  
1066 *of Fluid Mechanics*, *781*, 261–275. doi: <https://doi.org/10.1017/jfm.2015.462>  
1067 Xu, G., Jackson, D., Bemis, K., & Rona, P. (2013). Observations of the volume flux  
1068 of a seafloor hydrothermal plume using an acoustic imaging sonar. *Geochem-*  
1069 *istry, Geophysics, Geosystems*, *14*(7), 2369–2382. doi: [https://doi.org/10.1002/](https://doi.org/10.1002/ggge.20177)  
1070 [ggge.20177](https://doi.org/10.1002/ggge.20177)  
1071 Xu, G., McGillicuddy Jr, D., Mills, S., & Mullineaux, L. (2018). Dispersal of  
1072 hydrothermal vent larvae at east pacific rise 9–10 n segment. *Journal of Geo-*  
1073 *physical Research: Oceans*, *123*(11), 7877–7895. doi: [https://doi.org/10.1029/](https://doi.org/10.1029/2018JC014290)  
1074 [2018JC014290](https://doi.org/10.1029/2018JC014290)